

1 Response of the tropical Pacific Ocean to El Niño versus global warming

2 *Fukai Liu¹, Yiyong Luo¹, Jian Lu², and Xiuquan Wan¹*

3

4 ¹Physical Oceanography Laboratory, Ocean University of China, Qingdao, China

5 ²Atmospheric Sciences & Global Change Division, Pacific Northwest National Laboratory, WA, USA

6

7

8

9

10

11

12

13

14

15 Corresponding author:

16 Yiyong Luo

17 Physical Oceanography Laboratory

18 Ocean University of China

19 238 Songling Road

20 Qingdao 266100, China

21 Email: yiyongluo@ouc.edu.cn

22
23
24
25
26
27
28
29
30
31
32
33
34
35
36
37
38
39
40
41

Abstract

Climate models project an El Niño-like SST response in the tropical Pacific Ocean to global warming (GW). By employing the Community Earth System Model (CESM) and applying an overriding technique to its ocean component, Parallel Ocean Program version 2 (POP2), this study investigates the similarity and difference of formation mechanism for the changes in the tropical Pacific Ocean under El Niño and GW. Results show that, despite sharing some similarities between the two scenarios, there are many significant distinctions between GW and El Niño: 1) the phase locking of the seasonal cycle reduction is more notable under GW compared with El Niño, implying more extreme El Niño events in the future; 2) in contrast to the penetration of the equatorial subsurface temperature anomaly that appears to propagate in the form of an oceanic equatorial upwelling Kelvin wave during El Niño, the GW-induced subsurface temperature anomaly manifest in the form of off-equatorial upwelling Rossby waves; 3) while significant across-equator northward heat transport (NHT) is induced by the wind stress anomalies associated with El Niño, little NHT is found at the equator due to a symmetric change in the shallow meridional overturning circulation that appears to be weakened in both North and South Pacific under GW; and 4) the maintaining mechanisms for the eastern equatorial Pacific warming are also substantially different.

Key words: Tropical Pacific Ocean; Global warming; El Niño; El Niño-like response.

42 **1. Introduction**

43 El Niño-Southern Oscillation (ENSO) is the leading mode of the interannual variability in
44 the Earth's climate system and has significant impacts on climate variability across much of
45 the globe. The warm phase of ENSO, or El Niño, is characterized by unusually warm ocean
46 temperature in the eastern equatorial Pacific (EEP), accompanying with an eastward shift of
47 the warm pool and rainfall, a reduction of the equatorial easterly winds, and a flattening of
48 the zonal thermocline slope (Rasmusson et al., 1982, Neelin et al., 1998; Wang and
49 McPhaden, 2000, 2001). Ocean-atmosphere coupling is a major cause of ENSO (Bjerknes,
50 1969; Zebiak and Cane, 1987), and the thermocline-SST positive feedback (i.e., the Bjerknes
51 feedback) is believed to be responsible for the onset and strengthening of El Niño. For the
52 termination of El Niño or its transition to the cold phase (i.e., La Niña), four negative
53 feedbacks have been proposed: the delayed oscillator (Suarez and Schopf, 1988; Battisti,
54 1988), discharge–recharge oscillator (Jin, 1996, 1997a and 1997b), western Pacific oscillator
55 (Wang and Weisberg, 1994; Weisberg and Wang, 1997), and advective–reflective oscillator
56 (Picaut et al., 1996, 1997). Due to the complexity of the evolution of ENSO, more than one
57 of the above negative feedbacks may be operating in a variety of combinations (Wang and
58 Picaut, 2004).

59

60 On the other hand, a majority of climate models (e.g., Liu et al 2005, Held and Soden 2006,
61 Xie et al 2010, Lu and Zhao 2012) has projected that the mean climate condition in the
62 tropical Pacific Ocean shifts towards an ‘El Niño-like’ state under global warming (GW),
63 with features such as an enhanced warming in the EEP, a shoaling of the thermocline in the
64 western equatorial Pacific (WEP), and a weakening of the south equatorial current (SEC).
65 These oceanic changes are generally interpreted as a direct response to a weakening of
66 easterly wind anomalies in the equatorial Pacific associated with the slowdown of the Walker
67 circulation, a robust signature of the atmospheric response to GW (e.g., Vecchi and Soden,
68 2007). However, it has been found that the physical mechanisms that drive tropical Pacific
69 climate change depart substantially from the ENSO analogy (DiNezio et al., 2009). Recently,

70 Luo et al. (2014) demonstrated that the weakening of the equatorial easterlies contributes
71 only marginally to the El Niño-like SST warming pattern under GW, which in stead appears
72 to be mainly controlled by the air-sea thermal interaction. Their model experiments revealed
73 further differences between the El Niño-like response to GW and El Niño: although in both
74 cases the upwelling in the EEP weakens, the total effect of vertical temperature advection in
75 the mixed layer is opposite, cooling for GW (due to enhanced upper-ocean stratification) but
76 heating for El Niño.

77

78 Since the shift of mean climate conditions toward the ‘El Niño-like’ state could alter the
79 amplitude, frequency, seasonal timing or spatial patterns of ENSO and then affect a range of
80 weather phenomena (Collins et al., 2010; Vecchi and Wittenberg, 2010; DiNezio et al., 2012),
81 it is of great importance to understand the differences and similarities of underlying
82 formation mechanisms for the tropical Pacific between GW and El Niño. However, it is still
83 debatable as to whether ENSO activity will be weakened or strengthened, owing to the
84 delicate balance of competing processes under GW. For example, an enhanced thermal
85 stratification and associated shallower thermocline along the equatorial Pacific tends to
86 destabilize the tropical coupling system, increase the sensitivity of SST to an anomaly in
87 thermocline or wind stress, and thus increase the amplitude of ENSO; on the other hand, the
88 higher Newtonian damping on the SST (Xie et al. 2010) and more stable atmosphere due to
89 a less vigorous zonal circulation tend to reduce the amplitude of ENSO (Philip and
90 Oldenborgh, 2006; Zhang et al., 2008)

91

92 These existing studies above focused mainly on the annual mean state differences between
93 GW and El Niño, and little attention has been given to their different seasonalities. The
94 seasonal cycle can contribute to the irregularity and phase locking of ENSO, and the
95 intra-seasonal variability can be a source of both ENSO variability and irregularity (Wang
96 and Picaut, 2004). In addition, the seasonal cycle is responsible for around 90% of the total
97 surface temperature variance on annual and longer time scales (Dwyer et al. 2012). In this

98 study we investigate the similarity and difference of the SST formation processes between
99 GW and El Niño, with a focus on their seasonal evolution. To this end, we conducted a suite
100 of numerical experiments using the NCAR's Community Earth System Model version 1.1
101 (CESM1.1) and its ocean component, the Parallel Ocean Program version 2 (POP2). In
102 particular, an overriding technique is employed as a diagnostic tool to isolate and evaluate
103 the role of wind changes in the robust features of the tropical Pacific Ocean under GW
104 versus El Niño. The overriding technique enables us to isolate individual feedbacks (e.g., the
105 wind-thermocline-SST feedback) from other factors (Lu and Zhao, 2012; Luo et al., 2014).
106 In addition, a heat budget analysis will be performed to further diagnose the mechanisms of
107 the SST formation under GW versus El Niño.

108

109 The rest of the paper is structured as follows. The model and numerical experiments are
110 described in the next section. In section 3, the methods used to calculate energy budget and
111 construct an El Niño composite are explained. In section 4, we compare the oceanic and
112 atmospheric changes over the tropical Pacific between GW and El Niño, including mean
113 patterns, seasonal evolutions, subsurface changes and northward heat transports. The results
114 of heat budget analysis are presented in section 5. Finally, a summary and a discussion of our
115 findings are given in section 6.

116

117 **2. Model and experiment design**

118 The main modeling tool for this study is CESM1.1, which is comprised of the Community
119 Atmospheric Model version 5 (CAM5), the Community Land Model version 4 (CLM4) and
120 the POP2 ocean component. The horizontal resolution of CAM5 and CLM4 is 1.9° longitude x
121 1.9° latitude, with the atmospheric component having 30 vertical levels. The horizontal
122 resolution of the POP2 is nominal 1° , telescoped meridionally to $\sim 0.3^\circ$ at the equator.
123 Vertically, it has 60 uneven levels with the thickness varying from 10 m near the surface to
124 250 m near the bottom.

125

126 Initialized from the end of the historical experiment (1861-2005) available at NCAR, we
127 conduct a 94-year projection run under the Representative Concentration Pathway (RCP) 8.5
128 scenario from 2006 to 2099 using CESM1.1, and save its daily outputs of various oceanic
129 and atmospheric variables. This experiment is labeled “CPL85” (Table 1). GW-induced
130 linear trends are derived from least-squared linear fitting from this experiment. In addition,
131 the data from the CPL85 simulation will be used to construct an El Niño composite, the
132 procedure for which will be explained in details in section 3.

133

134 Applying the daily surface atmospheric forcing fields (including winds, air temperature, air
135 pressure, specific humidity, precipitation rate, air density, and net short-wave and downward
136 long-wave radiations) from CPL85, the POP2 is then integrated for 94 years from 2006 to
137 2099, and this experiment is called “FULL” (Table 1). Note that in POP2 bulk formulae are
138 used to calculate evaporation as well as latent and sensible heat fluxes. A comparison of the
139 SST trend in the tropics between CPL85 and FULL demonstrates that the signature of the
140 SST response in CPL85 is well reproduced by FULL, including an ‘El Niño-like’ warming
141 pattern in the tropical Pacific Ocean (see Figure 2 of Luo et al., 2014). As we are aware of
142 that the way how the ocean interacts with the atmosphere is changed in the ocean-alone
143 experiments and this might introduce a shock at year 2006 and an artificial trend as a result
144 of the adjustment to the shock, we conduct another experiment with POP2 driven repeatedly
145 by the same atmospheric fields from year 2006 for 94 years. This experiment serves as the
146 control run for the overriding experiments and is referred to as CTRL (Table 1).

147

148 In order to isolate the effect of changing wind stress (wind speed), experiment STRS (SPED)
149 is performed with the wind stress (wind speed) fixed at repeating annual cycle of year 2006
150 while all other fields being the same as FULL. The wind stress contribution to the oceanic
151 changes can be derived by subtracting STRS from FULL, and the wind speed contribution
152 by subtracting SPED from FULL, the latter reflecting the effect of wind speed on
153 evaporation through the bulk formula (referred to as Wind-Evaporation-SST or WES effect

154 hereafter). It should be stressed that this WES effect only accounts for the direct thermal
155 effect on ocean of the changing wind speed, not including the indirect feedbacks through the
156 atmospheric processes as the WES in the fully coupled model (Lu and Zhao, 2012). The
157 experiment WIND with both wind stress and wind speed fixed at year 2006 values is
158 conducted to assess the linearity of the oceanic response to the two aspects to wind forcing,
159 which turns out to hold accurately.

160

161 In brief, the wind stress effect (WS) can be deduced from FULL – STRS, the wind speed
162 effect (WES) from FULL – SPED, and the effect of warming in the absence of wind stress
163 and wind speed changes from WIND – CTRL, hereafter referred to as thermal warming
164 effect (TW). FULL – CTRL mimics the full response in the coupled CESM1.1,
165 encompassing all the effects above. Our analysis is based on monthly mean fields, and all El
166 Niño-induced anomalies are computed with respect to each experiment’s own climatology
167 while the GW-induced changes are the linear trends over 2006-2099 periods.

168

169 **3. Methods of analysis**

170 *3.1 Temperature budget equation*

171 A temperature budget analysis is performed to diagnose the leading maintaining mechanisms
172 for the SST anomalies revealed by the experiments. Since the 0-55 m layer temperature
173 (referred to as mixed layer temperature, MLT, hereafter) has very similar interannual
174 variability (not shown) to the SST, a fixed bottom at 55 m is chosen for the heat budget to
175 avoid entrainment terms. Reducing the number of terms eases interpretation but also reduces
176 potential error sources in the computation (Alory and Meyers, 2009). The temperature budget
177 equation is expressed as:

$$178 \quad T_t = H - uT_x - vT_y - wT_z + T_{diff} \quad (1)$$

179 where T_t represents the tendency of the mixed layer temperature (MLT); $H = (Q_0 -$
180 $Q_h)/(\rho_0 c_p h)$ is the net heat flux, in which Q_0 and Q_h are the heat fluxes at the surface

181 and heat penetration at the water depth of 55 m, respectively, and ρ_0 and c_p are the density
 182 and specific heat of sea water; $-uT_x$, $-vT_y$, and $-wT_z$ are the zonal, meridional, and
 183 vertical advection of temperature, respectively; and T_{diff} represents the sum of
 184 contributions from the horizontal and vertical diffusion, as well as the convergence of heat
 185 by the transient eddies. For brevity, it will be referred to as diffusion term hereafter. Since the
 186 diffusion and eddy terms are not stored as part of the model's outputs, we can only infer the
 187 values of T_{diff} as the residual of equation (1). A positive (negative) T_{diff} indicates a
 188 heating (cooling) effect by diffusion.

189

190 It is worthwhile to note that there is a significant negative correlation ($r = -0.68$) between
 191 diffusion and MLT anomaly in the EEP region (5 °S-5 °N, 130 °W-80 °W). This indicates that
 192 the diffusion acts to damp the MLT anomaly. Given this correlation, almost half of the
 193 variation in the diffusion term can be accounted for by the time series of the MLT. With the
 194 least squares fitting (Fig. 1), T_{diff} may be expressed in a Newtonian cooling form as
 195 follows:

$$196 \quad T_{diff}(t) = -0.192 \times T'(t) + 0.804 \quad (2)$$

197 where T' refers to the monthly MLT anomaly over the EEP region. The relationship (2) can
 198 be used to roughly estimate the effects of vertical and eddy diffusion from the evolution of
 199 the MLT in the EEP, the most important region over global oceans in terms of impacts on
 200 climate.

201

202 *3.2 Temperature budget balance*

203 Using the budget equation (1), we first evaluate the interannual variability of the MLT and the
 204 related processes. Figure 2 shows the annual mean values of heat budget terms over the WEP
 205 (135 °E-170 °E, 5 °S-5 °N) and EEP, and their corresponding climatological mean values over
 206 the 2006-2099 periods are listed in Table 2. They are computed from the monthly outputs
 207 from CPL85, and depict the interannual variability as well as the mean balance. It is found that

208 the main balance terms are different between the EEP and WEP. Over the EEP, the main
209 cooling term is the vertical advection ($-19.5\text{ }^{\circ}\text{C}$ per year), and the main warming terms are the
210 diffusion ($9.6\text{ }^{\circ}\text{C}$ per year) and net heat flux ($10.2\text{ }^{\circ}\text{C}$ per year), while both the zonal and
211 meridional advections has much less contribution to the heat balance. In the WEP region, the
212 main balance is maintained among the surface warming ($3.2\text{ }^{\circ}\text{C}$ per year) by the net heat flux,
213 the zonal advective cooling ($-2.0\text{ }^{\circ}\text{C}$ per year), and the vertical advective cooling ($-1.2\text{ }^{\circ}\text{C}$ per
214 year). The meridional advection and diffusion play a minor role for the heat balance there.

215

216 The simulated annual mean temperature tendency time series (T_t , expressed in black lines in
217 Fig. 2) and that reconstituted from the temporal integration of the sum of the all the explicit
218 terms [$d(H - uT_x - vT_y - wT_z)$, expressed in gray lines in Fig. 2] are highly correlated and
219 their correlation coefficient reaches 0.93 in both the WEP and EEP, suggesting that this heat
220 budget formulation without resolving explicitly the diffusion term can account for
221 considerable interannual variability of the MLT in the tropical Pacific Ocean. The difference
222 between the simulated and reconstituted temperature change (purple lines in Fig. 2) is an
223 estimate of the importance of the total diffusion-eddy processes, which turns out to be a
224 significant warming term over the EEP (with an average $\sim 9.6\text{ }^{\circ}\text{C}$ per year; Table 2). In addition,
225 its variation at the interannual scale is found to be comparable to that of the vertical advection
226 (upwelling), indicating that the diffusion and subgrid-scale mixing are important for the
227 closure of the interannual heat budget in the EEP.

228

229 *3.3 El Niño composite*

230 We construct an El Niño composite following the procedure of Huang et al (2012). After the
231 simulated time series from 2006–2009 in CPL85 are detrended to remove the GW signal, the
232 MLT anomaly over the Nino3.4 region ($170^{\circ}\text{W}\sim 120^{\circ}\text{W}$, $5^{\circ}\text{S} \sim 5^{\circ}\text{N}$) are obtained. In this
233 analysis, a criterion of $2\text{ }^{\circ}\text{C}$ of the anomaly is chosen to define an El Niño event, and 17 El
234 Niño events are identified during the 94-year simulation period (Fig. 3). Figure 4a shows the
235 seasonal evolution of their composite. The composite reaches its peak during the boreal

236 winter of year 00 and its magnitude is consistent with observations (e.g., Rasmusson and
237 Carpenter, 1982). For convenience of discussion, we divide the evolution of El Niño into
238 four different stages: (a) the development phase extending from Jan. to May of year 00; (b)
239 the peak phase from Jul. to Dec. of year 00; (c) the decay phase from Jan. to Jun. of year 01;
240 (d) the demise phase from Jul. to Dec. of year 01. In addition, to facilitate the comparison
241 between El Niño and GW, we define a 12-month "El Niño year" to be the average from July
242 of year 00 to June of year 01, thus the annual mean state of El Niño can be compared with
243 that of GW. As will be shown in section 4, the composite El Niño captures well the major
244 characteristics of the observed El Niño.

245

246 As the experiment of FULL – CTRL reproduces faithfully the interannual variability of
247 CPL8.5, we use the same 17 events as in CPL85 for the El Niño composite for the overriding
248 experiments. It is found that the evolution of the El Niño composite in CPL85 (Fig. 4a) is
249 well reproduced by FULL – CTRL (Fig. 4b), but with a slightly larger amplitude, likely due
250 to the lack of higher-than-daily-frequency air-sea fluxes in the ocean-alone experiments. The
251 WS effect plays a dominant role in the El Niño evolution (Fig. 4c), while the contribution
252 from the WES effect is negligible (Fig. 4d). Interestingly, in the absence of the wind stress
253 and wind speed changes, the TW effect can also produce weak El Niño events (Fig. 4e),
254 consistent with the notion of Clement et al. (2011) that El Niño-like variability can arise
255 solely from thermal coupling between the ocean and atmosphere without the Bjerknes
256 feedback.

257

258 The analysis in the following sections is based primarily on the CPL85 simulation, and the
259 overriding experiments will be used to further isolate the role of individual feedbacks in the
260 formation of El Niño and GW. Due to the high similarities between CPL85 and FULL –
261 CTRL, all the discussions related to the CPL85 run can be carried over to FULL – CTRL.
262 Besides, since the magnitude of the modeled WES-induced oceanic change is negligible (Fig.
263 4d), we will not show the results of FULL – SPED (WES feedback) in the rest of this paper.

264

265 To facilitate the comparison of the SST pattern with El Niño, the basin mean warming
266 (averaged over 20°S – 20°N in the Pacific Ocean) in GW is first removed and the resultant
267 anomalies are then rescaled to have a maximum of 3 °C--the maximum MLT anomaly of El
268 Niño. In so doing, MLT warming less than the basin mean warming is represented by a
269 cooling in Figs. 5b, 6b and 7b. Note the rescaling is only applied to GW-induced MLT
270 anomalies (i.e., Figs. 5b, 6b and 7b), and the temperature anomalies along the equator on the
271 right panels of Fig.8 are original values.

272

273 **4. Oceanic and atmospheric changes in the tropical Pacific**

274 *4.1 Mean patterns*

275 Various features of the El Niño composite are shown on the left panels of Fig. 5. In
276 comparison with observations (e.g. Rasmusson and Carpenter, 1982; Wang and McPhaden,
277 2000 and 2001), the CESM model shows considerable realism in simulating the El Niño
278 spatial distributions over the tropical Pacific. Warm MLT anomalies appears in the EEP with
279 maximum warming ~3 °C around 100°W (Fig. 5a), accompanied by easterly wind anomalies
280 (Fig. 5c) in the central equator as well as less net heat flux along the entire equator (Fig.11g).
281 The oceanic changes also include a weakening of the westward SEC (Fig. 5e), a slowdown
282 of the Tropical Cells (TCs) (Fig. 11a) and a reduction of the upwelling along the equator (Fig.
283 5g). A note is that over the EEP region the westward anomalous current (color in Fig. 5e)
284 appears to counter the eastward mean current (contours in Fig. 5e), likely due to that fact that
285 the modeled thermocline is shallower than 55 m and the change of the 55-m mean current is
286 dominated by that of the equatorial undercurrent (EUC). In the EEP, another signature of
287 change is a significant reduction of the upper-ocean stratification (Fig. 5i) due to a deepening
288 of the thermocline there (Fig. 8i).

289

290 GW-induced changes are shown on the right panels of Fig. 5. The MLT exhibits a clear El
291 Niño-like pattern in the tropical Pacific (Fig. 5b), with enhanced warming in the central and

292 eastern equator and less warming in the west. The differences between the GW pattern and
293 that of the El Niño are also salient. For example, the El Niño warming extends to $\pm 15^\circ$
294 latitude, and displays a greater symmetry about the equator than the GW pattern. For the
295 latter, however, there is a pronounced cooling (lack of warming) in the southeastern tropical
296 Pacific, which has no counterpart in the northern tropical Pacific. This asymmetry has been
297 suggested to be rooted in the asymmetry of the pattern of the change of the trade winds (see
298 Fig. 5d) through the WES feedback (Xie et al., 2010, Lu and Zhao, 2012; Luo et al., 2014).

299

300 In addition, the westerly anomalies along the equator under GW are found to shift eastward
301 in comparison with the those during El Niño (compared Fig. 5d to Fig.5c), with the center of
302 the anomalies around 120°W in the former but around 160°W in the latter. The zonal shift of
303 the wind stress plays a decisive role in the oceanic anomalous patterns along the equator (An
304 and Wang, 2000). For example, in response to the shift of the weakened easterlies, the
305 GW-induced weakening of the SEC is more significant in the eastern equatorial region
306 compared to that during El Niño, in which the maximum weakening appears to be around the
307 central equatorial region (comparing Fig. 5f to Fig. 5e).

308

309 The most striking difference between GW and El Niño may be the upper-ocean stratification
310 in the EEP, which is enhanced under GW (Fig. 5j) but weakened under El Niño (Fig. 5i). The
311 overriding experiments reveal that the weakening of the stratification during El Niño is due
312 mainly to the WS effect (Fig. 7c), in agreement with previous studies (Rasmusson and
313 Carpenter, 1982; Neelin et al., 1998; Wang and McPhaden, 2000 and 2001). Under GW,
314 however, both the WS and the TW effects appear to be responsible for the enhanced
315 stratification (Fig. 7d). More specifically, during El Niño, the weaker-than-normal easterlies
316 along the equator deepen the thermocline and induce larger warming in the subsurface than
317 surface in the EEP (Fig. 8i), thus reducing the temperature gradient in the vertical there.
318 However, the GW scenario produces a more stratified upper layer due to an ocean warming
319 that is greater near the surface and decreasing with depth (Fig. 8j) (Luo et al., 2009). These

320 changes in stratification will be further discussed together with the vertical velocity change
321 in section 5.

322

323 *4.2 Seasonal evolution*

324 The seasonal evolutions of the MLT and the related circulation features along the equator are
325 shown in Fig. 6 for El Niño and GW, respectively. As in the observations and previous
326 modeling studies (e.g. Zhang et al., 2007; Huang et al., 2010 and 2012), during El Niño,
327 westerly anomalies start to build up west of dateline in the El Niño development phase,
328 propagate eastward and strengthen in the following months, and then reach the peak
329 magnitude around Dec. of year 00 (Fig. 6c). In company with the evolution of the wind
330 anomalies, the oceanic response include an enhanced MLT warming (Fig. 6a), a reduction of
331 SEC (Fig. 6e), and a weakening of both upwelling (Fig. 6g) and upper-ocean stratification
332 (Fig. 6i) during the El Niño development phase, and these changes reach their maxima
333 around the peak phase of El Niño. These are followed by a delayed basin warming of the
334 Indian Ocean, that forces a baroclinic atmospheric Kelvin wave into the western Pacific,
335 causing the transition from the anomalous westerly winds to easterly winds over the WEP
336 (e.g., Okumura et al., 2011; Wang and McPhaden, 2000; Wang and Zhang, 2002). The
337 gradual weakening of the dominant westerly anomalies along the equatorial Pacific leads to
338 the transition from El Niño to La Niña during year 01. The major contribution of the wind
339 changes during El Niño described above is further confirmed by the results of our overriding
340 experiments (Fig. 7a), that is, the WS effect plays an important role for the magnitude as well
341 as seasonal evolution of MLT anomaly over the equatorial Pacific, while the TW effect
342 makes only a minor contribution to the equatorial warming as well as its seasonal evolution.

343

344 The GW-induced seasonal evolution of MLT and wind anomalies in the tropical Pacific
345 differs from that of El Niño on many aspects. Under GW, the anomalous westerly propagates
346 westward from the eastern to central equatorial Pacific during July of year 00 to January of
347 year 01 (Fig. 6d). In response to the wind stress change, the maximum warming signal is also

348 found to propagate correspondingly but with a lag of about 1-2 months (Fig. 6b). The
349 overriding experiments help isolate the role of individual feedback for the warming and its
350 propagation. Over the EEP region (Fig. 7b), the most striking feature is that the seasonal
351 variation of the MLT due to the WS effect is just the opposite to that due to the TW effect
352 (their correlation $r = -0.90$), e.g., the WS-induced warming reaches a maximum during
353 May-Jul when the warming resulting from the TW effect happens to be a minimum. Their
354 combined effects lead to small seasonal variation amplitude over the EEP region, which
355 seems to follow the anomalous seasonal evolution induced by the change of WS (their
356 correlation $r = 0.67$). Also, the seasonal evolution of MLT is characterized by an ‘M’-shaped
357 pattern, with two peaks in Apr. and Oct. respectively, which will be examined in detail
358 through the heat budget analysis later in section 5. This above result about the seasonal MLT
359 analysis complements the work by Luo et al. (2014), who focused on the annual mean
360 response in the tropical Pacific to GW and found that only 20% of the annual warming in the
361 EEP can be attributed to the WS effect. The analysis here, on the other hand, indicates that
362 the WS effect is dominant in the seasonal evolution of the MLT response to GW in the
363 equatorial Pacific.

364

365 ENSO events tend to peak during boreal winter and can be viewed as a disruption of the
366 seasonal cycle (Fig. 6a). It can be seen that GW projects even more strongly on to a
367 weakening of the seasonal cycle of the MLT, expressed as greater warming during cold
368 months (boreal winter) in the central and eastern equatorial Pacific (Fig. 6b). Note that the
369 response of the seasonal cycle of the tropical Pacific SST to global warming could be
370 model-dependent. For example, Jia and Wu (2013) found an enhanced seasonal cycle of SST
371 in the equatorial Pacific in response to GW in a simple coupled model, while Zelle et al.
372 (2005) found no obvious changes in the SST seasonal cycle from an earlier version of the
373 community climate model.

374

375 Notwithstanding the model sensitivity, our overriding experiments helps to identify the

376 source of the change of the seasonal cycle in both MLT and the tropical Pacific circulation:
377 the reduction during El Niño is dominated by WS effect (Fig. 7a), while that under GW is
378 resulted from the superposition of the WS and TW effects (Fig. 7b). In addition to the MLT,
379 under GW, other near-surface variables (such as zonal wind stress, zonal current, vertical
380 velocity and mixed layer stratification) also demonstrate notable reductions in seasonal cycle
381 that are strongly phase-locked to the mean seasonal cycle especially in the central and
382 eastern Pacific (right panels of Fig. 6). In comparison, however, their reductions during El
383 Niño are less phase-locked. Take vertical velocity for example, the GW-induced
384 downwelling reaches a maximum during boreal winter when the climatological vertical
385 velocity happens to be largest upward, while the downwelling induced by El Niño is about 2
386 months earlier and is somewhat westward shifted (Figs. 6g and 6h).

387

388 *4.3 Subsurface changes*

389 Substantial differences between El Niño and GW are also found at the subsurface in the
390 equatorial Pacific. The model reproduces well the major features of the thermocline change
391 in the tropical Pacific Ocean typical to El Niño (Wang and McPhaden, 2000 and 2001),
392 including a shoaling in the west and a deepening in the east, i.e., in a form of a seesaw during
393 much of the El Niño year (Fig. 8i). As the development phase of the El Niño cycle proceeds,
394 a westerly wind anomaly (Fig. 6c) results in anomalous eastward current (Fig. 6e) and
395 downwelling (Fig. 6g) east of 150°E through anomalous Ekman convergence, leading to
396 positive temperature anomaly at subsurface and the deepening of the thermocline in the
397 eastern Pacific. Then, this anomaly gradually amplifies and expands, and reaches a
398 maximum in Oct.-Dec. of year 00 (Fig. 8c). During this process, a cold subsurface
399 temperature anomaly also starts to develop in the western Pacific in order to compensate for
400 upwelling and the eastward current near the surface, and the thermocline water further
401 diverges and upwells, resulting in a significant cooling at subsurface and a shoaling of the
402 thermocline in the decay phase of El Niño. This anomalous cooling gradually propagates
403 eastward and upward to the eastern Pacific and replaces the warm anomaly during demise

404 phase, and then leads to a La Niña. As in the observations (Ohba and Ueda, 2007), the
405 penetration of the subsurface temperature anomaly appears in the form of an upwelling
406 oceanic equatorial Kelvin wave, which is forced by the anomalous easterly winds over the
407 western Pacific.

408

409 Under GW, however, the subsurface change is featured with an overall shoaling of the
410 equatorial thermocline, with more shoaling in the central and west together with a cooling
411 there (Fig. 8j). The shoaling of the thermocline in the east is resulted from a more stratified
412 upper layer due to ocean warming that is greater near the surface and decreasing with depth
413 (Luo et al., 2009), while the shoaling as well as the associated cooling in the central and west
414 Pacific arise mainly from the WS effect (as found in Luo et al. 2014), that can be
415 conveniently explained by the relaxation of the equatorial easterlies associated with the
416 slowdown of Walker circulation (Vecchi and Soden 2007). Another difference from El Niño
417 is that the seasonal evolution of the subsurface cooling in the equatorial Pacific can not be
418 characterized by a Kelvin wave propagation (right panels of Fig. 8). In stead, we find hints of
419 westward propagation of upwelling Rossby waves off the equator under GW (not shown).

420

421 *4.4 Northward heat transport*

422 Meridional heat transport is one of the most fundamental properties of the climate system
423 (Hazeleger et al., 2004). Here we examine the changes in the annual mean northward heat
424 transport (NHT) for the Pacific Ocean resulting from both El Niño and GW (Fig. 9). The
425 climatological NHT appears to have a high degree of inter-hemispheric anti-symmetry with
426 its sign reversed at the equator. Its peak values are 0.8 PW around 15°N and -0.9 PW around
427 15°S respectively, which are within the uncertainty range found by Trenberth and Caron
428 (2001). This NHT dipole is believed to be associated with the shallow meridional
429 overturning circulation (MOC) in the Pacific (McPhaden and Zhang, 2002), i.e., the
430 Subtropical Cells (STCs; McCreary and Lu, 1994) and its equatorial components, the TCs
431 (Perez and Kessler, 2009). While the TCs takes surface water away from the equator and

432 then recirculates vertically within the tropics, the STCs transports warmer water out of the
433 tropics within the surface layer and brings colder water from the subtropics back to the
434 equator in the thermocline (contours in Fig. 10).

435

436 During El Niño, it is found that the NHT increases greatly in the tropics from 10 °S to 20 °N,
437 with the maximum of ~0.9 PW at 7 °N, and decreases north of 20 °N and between 10 °S and
438 30 °S. The above response of the NHT is related to the changes in the Pacific shallow MOC
439 during El Niño (Fig. 10a), i.e., the STCs both in the north and south appear to spin up but the
440 TC in the south slows down significantly. The overriding experiments reveal that the El
441 Niño-induced NHT change is due mainly to the WS effect (Fig. 9b) that is further confirmed
442 by the MOC response to the WS change during El Niño (Fig. 10c).

443

444 Under GW, however, it is found that the response of the NHT is not so significant in
445 comparison with El Niño, and appears to be anti-symmetric about the equator with a
446 decrease in the northern hemisphere but an increase in the southern hemisphere (Fig. 9a).
447 This change of the NHT represents a reduction of the poleward transports in both
448 hemispheres, which is again consistent with the symmetric change in MOC that appears to
449 be weakened in both hemispheres under GW (Fig. 10b). According to the overriding
450 experiments, the reduction in the north is due mainly to the weakened trade winds that lead
451 to a slowdown of the northern STC, while the reduction in the south is caused by the
452 superposition of the WS change and the TW effect (Figs. 10d and 10f). The strengthening of
453 the southern STC due to the intensified southeast trade winds (Fig. 10d) is overwhelmed by
454 the weakening resulting from the TW effect (Fig. 10f), leaving an overall weakened STC
455 (Fig. 10b) and thus a positive (northward) NHT anomaly in the South Pacific (Fig. 9a).

456

457 The reduced poleward heat transport by the tropical Pacific, if acting in isolation, would
458 induce a net heating to the atmosphere, driving a stronger Hadley cell in the atmosphere (see
459 also Feldl and Bordoni, 2015). This might be the underlying mechanism for why overall the

460 Hadley cell weakens more in the slab model simulation than in the climate models coupled
461 with full ocean dynamics under increasing CO₂ forcing (G. Vecchi, 2007, personal
462 communication).

463

464 **5. Analysis of mixed layer heat budget**

465 In this section we analyze each term on the right hand side of equation (1) and examine their
466 responses to El Niño versus GW, respectively. Figure 11 shows the annual-mean forcing
467 terms for the tendency of MLT during El Niño and GW. It is found that there are substantial
468 differences on the major balance terms as well as their roles that maintain the warming in the
469 EEP. During El Niño, they are vertical advection (warming), net heat flux (cooling) and
470 diffusion (cooling). Under GW, however, the most prominent terms in the balance are the
471 cooling from vertical advection and warming from diffusion. More details are discussed
472 below.

473

474 *5.1 Vertical advection*

475 In the balance of the climatological state, the vertical advection is the major cooling term
476 over the EEP region (contours in Fig. 11a; Table 2), resulting from wind-induced strong
477 upwelling (contours in Fig. 5g) and large vertical temperature gradients (contours in Fig. 5i).
478 In the western and central equatorial Pacific, while the vertical advection is still a source of
479 cooling to the surface layer, its contribution is the same order of magnitude as the zonal and
480 meridional advection (Table 2).

481

482 In agreement with previous observational studies of the ENSO cycle (e.g., Wang and
483 McPhaden, 2000; 2001), the reduction of cold vertical advection plays a critical role for the
484 anomalous surface warming in the EEP (Fig. 11a), dominating the development and decay of
485 El Niño events (compared Fig. 12a with Fig. 12c). More specifically, the anomalous vertical
486 advection is resulted from both decreased vertical velocity (Fig. 6g) and weakened
487 stratification (Fig. 6i), with the latter playing a larger role. The decrease of the vertical

488 velocity is due to anomalous Ekman convergence from the reduction of the surface easterly,
489 while the weakening of the stratification is due to the deepening of the thermocline. However,
490 both changes are resulted from the weakened easterlies along the equator. This is confirmed
491 by the overriding experiments, which reveals that the WS change dominates overwhelmingly
492 the magnitude and seasonal evolution of the vertical advection while the TW effect tends to
493 damp the effect from the WS change (Fig. 13c).

494

495 In sharp contrast, the response of the vertical advection to GW exerts a cooling effect on the
496 surface layer in the central and eastern equatorial region (Fig. 11b). The cooling results from
497 the significantly enhanced stratification (Fig. 5j), despite the reduced vertical velocity
498 induced by the weakened equatorial easterlies under GW (Fig. 5h). The important controlling
499 role of the stratification for the vertical advection is further confirmed by its seasonal
500 evolution: the vertical advection (Fig. 12d) evolves synchronously with the stratification (Fig.
501 6j), and the anomalous warming induced by vertical advection in Mar. leads to the first T_t
502 maxima over the EEP (Fig. 13b), while the second T_t maxima in Oct. is from other budget
503 terms including the zonal and meridional advection, net heat flux as well as diffusion (Figs.
504 13f-13l). The overriding experiments further reveal that, unlike El Niño, both the WS and
505 TW effects are important in shaping the seasonal cycle of the EEP response to GW (Fig. 13d).
506 However, as far as the quantitative contribution to the phase evolution of the GW response is
507 concerned, WS effect seems more prevalent (Table 3).

508

509 *5.2 Zonal advection*

510 The effect zonal advection on the budget is characteristic of a dipole, with a cooling over the
511 western and central equatorial Pacific and a warming over the EEP (contours in Fig. 11c;
512 Table 2), owing to the negative zonal temperature gradient along the entire equator (contours
513 in Fig. 5a) and the opposite sign of zonal current between west and east of 130°W (contours
514 in Fig. 5e). As mentioned previously, the latter is due to the shallow EUC over the EEP
515 region (see Johnson et al. 2001 for the corresponding observational feature) .

516

517 We find that El Niño induces a warming anomaly of the zonal advection in the western and
518 central equatorial Pacific but a cooling anomaly in the EEP (Fig. 11c). This result is
519 consistent with the modeling work by Huang et al. (2012) but with different mechanism. In
520 our analysis, the warm zonal advection over the western and central equator is resulted from
521 the decrease of both zonal surface current and temperature gradient associated with the
522 weakened easterlies, and the cooling over the eastern equator is due to the anomalous
523 westward zonal currents there. In the study of Huang et al. (2012), however, it is the opposite
524 zonal gradient of anomalous temperature rather than anomalous surface current that
525 determines the reversal of the sign of anomalous zonal advection between west and east of
526 110°W. Nevertheless, the anomalous zonal advection is a major warming term in the western
527 and central Pacific and its seasonal evolution is in phase with the evolution of T_t (compared
528 Fig. 12e to Fig. 12a), indicating its important role in the surface heat balance there, which is
529 consistent with previous studies (McPhaden and Picaut 1990; Picaut and Delcroix 1995;
530 Picaut et al. 1996). In addition, the contribution from zonal advection to the negative peak of
531 T_t over the EEP region is comparable with that from vertical advection during the decay
532 phase of El Niño (compared Fig. 13e with Fig. 13c), indicating its importance to the
533 transition of ENSO phase. The overriding experiments further confirm the evolution of the
534 anomalous zonal advection in the EEP is dominated by the WS change (Fig. 13e).

535

536 The changing pattern of the zonal advection in the western and central Pacific under GW
537 (Figs. 11d and 12f) is similar to what happens during El Niño (Figs. 11c and 12e). Over the
538 EEP, however, instead of a cooling factor during El Niño, it appears to be a minor warming
539 owing to the eastward shift of the weakened easterlies under GW. Additional difference from
540 El Niño revealed by the overriding experiments is that the zonal advection in the EEP under
541 GW is induced by a combination of the WS effect and the TW effect (Fig. 13f). Note that the
542 strong anti-correlation between the WS- and TW-induced zonal advective changes ($r = -0.81$)
543 indicates a cancellation between the two effects (Table 3).

544

545 *5.3 Meridional advection*

546 The meridional advection cools the equatorial upper ocean and is in the same order of
547 magnitude as the zonal advection (contours in Fig. 11e). The meridional advection around
548 the equator is associated with the TCs (contours in Fig. 10a), which transports relatively cold
549 water out of the equator in the surface layer.

550

551 During El Niño, the cooling effect of the meridional advection is reduced, and the maximum
552 reduction appears a few degrees latitude off the equator (Fig. 11e), resulting from a
553 weakening of both the meridional temperature gradients associated with the enhanced
554 equatorial SST and the Ekman divergence (Fig. 10a) associated with the weaker easterlies
555 (Fig. 5c). Figure 12g shows that the anomalous meridional advection contributes to the
556 warming in the central and western Pacific that is in the same order of magnitude as the
557 anomalous zonal advection. The overriding experiments further reveal the dominant role of
558 the WS change in the anomalous meridional advection during El Niño (Fig. 13g).

559

560 GW also leads to a reduction of the meridional advection with its maxima off the equator by
561 a few degrees latitude. However, their locations move eastward in direct response to the
562 eastward shift of the weakened easterlies relative to that of El Niño. Under GW, in addition,
563 the anomalous meridional advection appears to be a warming source to the EEP and plays a
564 more significant role for the heat balance there than the anomalous zonal advection (Figs. 11f
565 and 12h). The strong correlations between full response and WS and TW effects ($r = 0.81$
566 and 0.77 , respectively) reveal that both effects may work cooperatively to drive the changes
567 in meridional advection under GW (Fig. 13h).

568

569 *5.4 Net heat flux*

570 The net surface heat flux in the climatology is a prominent warming effect for the mixed
571 layer in the entire equatorial Pacific, with a maximum exceeding $10\text{ }^{\circ}\text{C}/\text{year}$ at the eastern

572 equatorial Pacific (contours in Fig. 11g; Table 2).

573

574 During El Niño, the net heat flux is significantly reduced (implying heat leaving the ocean,
575 see Fig. 11g) and this change acts to damp the El Niño development due to its negative
576 correlation with MLT anomaly (Fig. 12i), as suggested by Wang and McPhaden (2000; 2001).
577 Our overriding experiments further suggest that the net heat flux would have reduced even
578 more were the ocean only under the forcing of the varying wind stress (without the thermal
579 feedback from the atmosphere) (Fig. 13i). This exemplifies the active role of the wind-driven
580 ocean dynamics in the surface energetics of the ENSO life cycle.

581

582 In contrast to the remarkable reduction of the net heat flux during El Niño, GW induces
583 much weaker annual mean change in the net heat flux (Fig. 11h), which is due to a
584 cancellation between the heating during Jul.-Dec. and the cooling during Jan.-Jun. (Fig. 12j).
585 The overriding experiments reveal that the thermal warming acts to inject warming into the
586 EEP region by average while the WS effect acts to extract heat from the ocean (Fig. 13j).
587 Unlike other ocean circulation related budget terms, the evolution of net heat flux response is
588 clearly dominated by TW effect (Table 3), which can be attributed to the dominant role of
589 air-sea thermal interaction in regulating the heat flux under GW.

590

591 *5.5 Diffusion*

592 Many previous studies ascribe an important role to vertical diffusion in the cold tongue
593 region (e.g., Harrison et al., 1990; Frankignoul et al., 1996; Wang and McPhaden, 2000;
594 Zhang and McPhaden, 2006; Zhang et al., 2007). Derived as the residual of the
595 thermodynamic equation in our research, the diffusion term acts as a primary warming
596 source to the equatorial Pacific with the maximum over the EEP region (contours in Fig. 11i;
597 Table 2).

598

599 During El Niño, the diffusive warming in the EEP is significantly decreased (Fig. 11i) and

600 the resultant cooling anomaly acts to compensate the strong vertical advective warming there
601 (Figs. 11a). This change in the diffusion may be explained as below. The ocean stability in
602 the upper layer of the EEP is decreased due to the greater anomalous warming at subsurface
603 than surface during El Niño (Fig. 8i). This stimulates the vertical diffusivity through a
604 Richardson number-dependent parameterization (Pacanowski and Philander, 1981) and, in
605 turn, the cold diffusive flux and entrainment, resulting in an anomalous cold vertical
606 diffusion (e.g., Yang et al., 2009). Seasonally, the diffusive cooling reaches the maximum
607 during the peak phase of El Niño over the EEP (Fig. 12k), and its seasonal variation is
608 mainly controlled by the WS effect (Fig. 13k).

609

610 Under GW, in stark contrast to El Niño, the anomalous diffusion is a warming effect in the
611 EEP (Fig. 11j), compensating the vertical advective cooling there (Fig. 11b). The diffusive
612 warming is resulted from greater warming in the surface than subsurface under GW, opposite
613 to what happens during El Niño as being explained in the last paragraph.

614

615 This compensation relationship between the diffusion and the vertical advection in our model
616 is further verified by their seasonal evolution (Figs. 12d and 12l), that is, when the
617 anomalous diffusion appears to be a cooling during Jan.-Mar., the anomalous vertical
618 advection is a warming; whereas when the anomalous diffusion is a warming during
619 Apr.-Dec., the anomaly vertical advection is a cooling. Further, the overriding experiments
620 reveal that the diffusive cooling anomaly during Jan.-Mar. is mainly driven by the WS
621 change, while its warming anomaly during Apr.-Dec. is largely controlled by the TW effect
622 (Fig. 13l). In terms of overall impact on the seasonality, the WS effect dominates as the
623 correlation between full response and WS induced diffusive changes attains 0.81 (Table 3).

624

625 Our above result of the heat budget analysis is in qualitative agreement with Jia and Wu
626 (2013) whose analysis were based upon an intermediate climate model with a full
627 atmospheric generation circulation model coupled to a 1.5-layer reduced-gravity ocean

628 model. For example, they also found that anomalous horizontal advection contributes to the
629 warming in the central and eastern Pacific, and a total contribution of changes in entrainment
630 and horizontal diffusion (comparable to the total contribution of vertical advection and
631 diffusion in our model) is to cool the central and eastern Pacific Ocean. However, there is a
632 difference regarding the role of surface net heat flux change: it contributes to the warming in
633 their model, while the annual mean contribution of the surface net flux is a weak cooling in
634 our model due to the cancellation among different months mentioned above.

635

636 **6. Summary and discussion**

637 There is increasing evidence that climate models tend to produce an El Niño-like sea surface
638 response in the tropical Pacific under the forcing of increasing concentration of greenhouse
639 gases. However, through a GW-El Niño inter-comparison analysis, we find that many of the
640 GW response features in the ocean as well as the related maintaining mechanisms turn out to
641 be quite different from a typical El Niño. As summarized in Fig. 14, the major similarities
642 and differences for the annual mean response are:

643

- 644 1. Both El Niño- and GW-induced patterns are featured with weakened equatorial trade
645 winds. In response to the slowdown of the trade winds, there appears to be
646 weakening in zonal SEC and meridional STC, enhancements in surface warming
647 over the EEP and shoaling of thermoclines in the WEP.
- 648 2. Associated with the eastward shift of the weakened easterlies, the surface-warming
649 center moves eastward and the weakening of the SEC are more significant in the EEP
650 under GW in contrast to El Niño.
- 651 3. Over the EEP region, GW induces greater warming in the surface than subsurface
652 while it is the other way around during El Niño. Taken together, GW-induced
653 response is characteristic more of an enhanced stratification in the upper ocean than a
654 shallower thermocline, whereas El Niño corresponds to a weaker upper ocean
655 stratification and a deeper thermocline.

656
657
658
659
660
661
662
663
664
665
666
667
668
669
670
671
672
673
674
675
676
677
678
679
680
681
682
683

By implementing a suite of numerical experiments, this study has focused on identifying the similarities and differences of their seasonal evolution as well as examining the underlying formation mechanisms in the tropical Pacific between GW and El Niño. In spite of sharing some similarities between the two scenarios, many significant distinctions under GW from El Niño are found and summarized as below:

1. The GW-induced surface warming propagates from the eastern to central Pacific during Jul.-Dec. when the El Niño-induced surface warming propagates eastward characterized by a downwelling equatorial Kelvin wave.
2. The upper ocean of the EEP is less stratified during the entire El Niño year with the maximum on its peak phase in winter while the GW-induced stratification is weakened in Jan-Mar and then strengthened the rest of the year.
3. There are an overall reduction in the amplitude of the seasonal cycle of the MLT under both El Niño and GW. However, the reduction of the seasonal cycle is closely phase-locked with the background mean seasonal cycle for the case of GW and manifested in both the equatorial wind and the wind-driven upper ocean circulation (such as zonal wind stress, vertical velocity and mixed layer stratification).
4. In contrast to the penetration of the equatorial subsurface temperature anomaly that appears to propagate in the form of an oceanic equatorial Kelvin wave during El Niño, the GW-induced subsurface temperature anomaly propagates in the form of upwelling Rossby waves.
5. In the context of the designed overriding experiments, the development of El Nino is resulted mainly from the WS effect is responsible for the evolution of El Niño, while the oceanic response to GW is due to a combination of both the WS change and the TW effect, with the former making a larger contribution to the seasonal cycle and the latter to the annual mean warming.
6. The integrated NHT also exhibits distinct characters between El Niño and GW in the

684 tropical Pacific. The wind stress anomalies associated with El Niño drive
685 across-equatorial cell between 10°S and 20°N, which transports net heat northward
686 across the equator. However, the GW-induced reduction of the poleward oceanic heat
687 transport is overall symmetric, with little cross-equatorial component.

688 7. There are substantial differences in the major balance terms that maintain the
689 warming over the EEP region. During El Niño, the balance is among vertical
690 advection (warming), net heat flux (cooling) and diffusion (cooling). Under GW,
691 however, the budget is balanced mainly between vertical advection (cooling) and
692 diffusion (warming).

693

694 To further validate the results here based on our own CESM run (i.e., the CPL85), three
695 members of RCP8.5 simulations with CESM are also obtained from NCAR. All the features
696 regarding El Niño and GW found from the CPL85 run are replicated and confirmed with the
697 NCAR ensemble simulations (now shown), suggesting that our modeling approach is reliable
698 for examining the oceanic response in the tropical Pacific to GW.

699

700 While the projected seasonal mean changes in the eastern Pacific (i.e., an El Niño-like
701 warming pattern) are largely consistent among different climate models, the changes in the
702 ENSO statistics are quite different. A recent study by Cai et al. (2014) suggested that,
703 although the total number of El Niño events does not appear to have a significant change due
704 to GW, the frequency of extreme El Niño events will increase substantially. Interestingly, our
705 CPL85 simulation seems to corroborate this notion (Fig. 3). If an extreme El Niño event is
706 defined as the MLT anomaly at Nino3.4 region exceeding 3.0 °C during the peak phase, its
707 frequency is found to double from about one event every 23 years during the first half of the
708 21st century (2 events from 2006 to 2052) to one every 12 years during the second half of the
709 21st century (4 events from 2053 to 2099). The increase of extreme El Niño events have
710 further been confirmed through the three ensemble members conducted by NCAR, in which
711 the number of extreme El Niño events increases from 6 in the first half of 21st century to 12

712 in the second half of 21st century. This increase may be associated with the El Niño-like
713 mean warming response under GW, i.e., more surface warming in the EEP than the
714 surrounding ocean waters, facilitating more occurrences of maximum SSTs, and hence
715 convection for a given SST anomaly (Cai et al., 2014). In addition, this may also be linked to
716 the reduction in the amplitude of the seasonal cycle, which usually implies a strong El Niño,
717 because when less energy is within the seasonal cycle, more is left for inter-annual signal
718 (Fedorov and Philander 2001; Guilyardi 2006).

719 The result that the WES feedback on the changes in the Pacific is negligible should be taken
720 with caution, since prescribing the atmospheric conditions in the ocean-alone setting
721 compromises the full WES effect, which can in turn feed back to the atmosphere (Lu and
722 Zhao, 2012). Further experiments with the CESM in partially coupled settings are underway
723 to tease out the specific effects of WES in the SST response of the tropical Pacific to global
724 warming.

725

726

Acknowledgements

727 This work is supported by NSFC (41376009 & 41221063) and NSF (AGS-1249173 &
728 AGS-1249145). Y. Luo would also like to acknowledge the support from the Zhufeng and
729 Taishan Projects of the Ocean University of China. J. Lu is supported by the Office of
730 Science of the U.S. Department of Energy as part of Regional and Global Climate Modeling
731 program.

732

733 **Reference**

- 734 An S Il, Wang B (2000) Interdecadal change of the structure of the ENSO mode and its
735 impact on the ENSO frequency. *J Clim* 13:2044–2055. doi:
736 10.1175/1520-0442(2000)013<2044:ICOTSO>2.0.CO;2
- 737 Alory G, Meyers G (2009) Warming of the Upper Equatorial Indian Ocean and Changes in
738 the Heat Budget (1960–99). *J Clim* 22:93–113. doi: 10.1175/2008JCLI2330.1
- 739 Battisti DS (1988) Dynamics and Thermodynamics of a Warming Event in a Coupled
740 Tropical Atmosphere–Ocean Model. *J. Atmos. Sci.* 45:2889–2919.
- 741 Bjerknes J (1969) Atmospheric Teleconnections From the Equatorial Pacific. *Mon Weather*
742 *Rev* 97:163–172. doi: 10.1175/1520-0493(1969)097<0163:ATFTEP>2.3.CO;2
- 743 Cai W, Borlace S, Lengaigne M, et al (2014) Increasing frequency of extreme El Niño events
744 due to greenhouse warming. *Nat Clim Chang* 5:1–6. doi: 10.1038/nclimate2100
- 745 Clement A, DiNezio P, Deser C (2011) Rethinking the ocean’s role in the Southern
746 Oscillation. *J Clim* 24:4056–4072. doi: 10.1175/2011JCLI3973.1
- 747 Collins M, An S-I, Cai W, et al (2010) The impact of global warming on the tropical Pacific
748 Ocean and El Niño. *Nat Geosci* 3:391–397. doi: 10.1038/ngeo868
- 749 DiNezio PN, Clement AC, Vecchi G a., et al (2009) Climate response of the equatorial
750 pacific to global warming. *J Clim* 22:4873–4892. doi: 10.1175/2009JCLI2982.1
- 751 Dinezio PN, Kirtman BP, Clement AC, et al (2012) Mean climate controls on the simulated
752 response of ENSO to increasing greenhouse gases. *J Clim* 25:7399–7420. doi:
753 10.1175/JCLI-D-11-00494.1
- 754 Dwyer JG, Biasutti M, Sobel AH (2012) Projected Changes in the Seasonal Cycle of Surface
755 Temperature. *J Clim* 25:6359–6374. doi: 10.1175/JCLI-D-11-00741.1
- 756 Fedorov A V., Philander SG (2001) A stability analysis of tropical ocean-atmosphere
757 interactions: Bridging measurements and theory for El Niño. *J Clim* 14:3086–3101. doi:
758 10.1175/1520-0442(2001)014<3086:ASAOTO>2.0.CO;2
- 759 Feldl N. and Bordoni B. (2015) Characterizing the Hadley circulation response through
760 regional climate feedbacks. *J. Clim.*, (submitted manuscript)

761 Frankignoul C, Bonjean F, Reverdin G (1996) Interannual variability of surface currents in
762 the tropical Pacific during 1987–1993. *J Geophys Res* 101:3629. doi:
763 10.1029/95JC03439

764 Guilyardi E, Wittenberg A, Fedorov A, et al (2009) Understanding El Niño in
765 ocean-atmosphere general circulation models: Progress and challenges. *Bull Am*
766 *Meteorol Soc* 90:325–340. doi: 10.1175/2008BAMS2387.1

767 Harrison DE, Giese BS, Sarachik ES (1990) Mechanisms of SST Change in the Equatorial
768 Waveguide during the 1982–83 ENSO. *J. Clim.* 3:173–188.

769 Hazeleger W, Seager R, Cane MA, Naik NH (2004) How Can Tropical Pacific Ocean Heat
770 Transport Vary? *J Phys Oceanogr* 34:320–333. doi:
771 10.1175/1520-0485(2004)034<0320:HCTPOH>2.0.CO;2

772 Held IM, Soden BJ (2006) Robust Responses of the Hydrological Cycle to Global Warming.
773 *J Clim* 19:5686–5699. doi: 10.1175/JCLI3990.1

774 Huang B, Xue Y, Zhang D, et al (2010) The NCEP GODAS Ocean Analysis of the Tropical
775 Pacific Mixed Layer Heat Budget on Seasonal to Interannual Time Scales. *J Clim*
776 23:4901–4925. doi: 10.1175/2010JCLI3373.1

777 Huang B, Xue Y, Wang H, et al (2012) Mixed layer heat budget of the El Niño in NCEP
778 climate forecast system. *Clim Dyn* 39:365–381. doi: 10.1007/s00382-011-1111-4

779 Jia F, Wu L (2013) A Study of Response of the Equatorial Pacific SST to Doubled-CO₂
780 Forcing in the Coupled CAM–1.5-Layer Reduced-Gravity Ocean Model. *J Phys*
781 *Oceanogr* 43:1288–1300. doi: 10.1175/JPO-D-12-0144.1

782 Jin F-F (1996) Tropical Ocean-Atmosphere Interaction, the Pacific Cold Tongue, and the El
783 Niño-Southern Oscillation. *Science* (80-) 274:76–78. doi:
784 10.1126/science.274.5284.76

785 Jin F-F (1997a) An Equatorial Ocean Recharge Paradigm for ENSO. Part I: Conceptual
786 Model. *J Atmos Sci* 54:811–829. doi:
787 10.1175/1520-0469(1997)054<0811:AEORPF>2.0.CO;2

788 Jin F-F (1997b) An Equatorial Ocean Recharge Paradigm for ENSO. Part II: A

789 Stripped-Down Coupled Model. *J Atmos Sci* 54:830–847. doi:
790 10.1175/1520-0469(1997)054<0830:AEORPF>2.0.CO;2

791 Johnson, G. C., M. J. McPhaden, E. Firing (2001) Equatorial Pacific Ocean Horizontal
792 Velocity, Divergence, and Upwelling*. *J. Phys. Oceanogr.*, 31, 839–849,
793 doi:10.1175/1520-0485(2001)031<0839:EPOHVD>2.0.CO;2.

794 Liu Z, Vavrus S, He F, et al (2005) Rethinking tropical ocean response to global warming:
795 The enhanced equatorial warming. *J Clim* 18:4684–4700. doi: 10.1175/JCLI3579.1

796 Lu J, Zhao B (2012) The role of oceanic feedback in the climate response to doubling CO₂. *J*
797 *Clim* 25:7544–7563. doi: 10.1175/JCLI-D-11-00712.1

798 Luo Y, Liu Q, Rothstein L (2009) Simulated response of North Pacific mode waters to global
799 warming. *Geophys Res Lett* 36:L23609. doi: 10.1029/2009GL040906

800 Luo Y, Lu J, Liu F, Liu W (2014) Understanding the El Niño-like oceanic response in the
801 tropical Pacific to global warming. *Clim Dyn.* doi: 10.1007/s00382-014-2448-2

802 McCreary Jr, J. P., Lu, P. (1994). Interaction between the subtropical and equatorial ocean
803 circulations: The subtropical cell. *Journal of Physical Oceanography*, 24(2), 466-497.

804 McPhaden MJ, Picaut J (1990) El Niño-southern oscillation displacements of the Western
805 equatorial pacific warm pool. *Science* 250:1385–8. doi:
806 10.1126/science.250.4986.1385

807 McPhaden MJ, Zhang D (2002) Slowdown of the meridional overturning circulation in the
808 upper Pacific Ocean. *Nature* 415:603–608. doi: 10.1038/415603a

809 Neelin JD, Battisti DS, Hirst AC, et al (1998) ENSO theory. *J Geophys Res* 103:14261. doi:
810 10.1029/97JC03424

811 Ohba M, Ueda H (2007) An Impact of SST Anomalies in the Indian Ocean in Acceleration of
812 the El Niño to La Niña Transition. *J Meteorol Soc Japan* 85:335–348. doi:
813 10.2151/jmsj.85.335

814 Okumura YM, Ohba M, Deser C, Ueda H (2011) A Proposed Mechanism for the
815 Asymmetric Duration of El Niño and La Niña. *J Clim* 24:3822–3829. doi:
816 10.1175/2011JCLI3999.1

817 Pacanowski RC, Philander SGH (1981) Parameterization of Vertical Mixing in Numerical
818 Models of Tropical Oceans. *J Phys Oceanogr* 11:1443–1451. doi:
819 10.1175/1520-0485(1981)011<1443:POVMIN>2.0.CO;2

820 Perez RC, Kessler WS (2009) Three-Dimensional Structure of Tropical Cells in the Central
821 Equatorial Pacific Ocean*. *J Phys Oceanogr* 39:27–49. doi: 10.1175/2008JPO4029.1

822 Philip SY, van Oldenborgh GJ (2006) Shifts in ENSO coupling processes under global
823 warming. *Geophys Res Lett* 33:1–5. doi: 10.1029/2006GL026196

824 Picaut J, Delcroix T (1995) Equatorial wave sequence associated with warm pool
825 displacements during the 1986–1989 El Niño-La Niña. *J. Geophys. Res.* 100:18393.

826 Picaut J, Ioualalen M, Menkes C, et al (1996) Mechanism of the Zonal Displacements of the
827 Pacific Warm Pool: Implications for ENSO. *Science* 274:1486–1489.

828 Picaut J, F Masia, and Y duPenhoat (1997) An Advective-Reflective Conceptual Model for
829 the Oscillatory Nature of the ENSO. *Science* (80-) 277:663–666. doi:
830 10.1126/science.277.5326.663

831 Rasmusson EM, Carpenter TH (1982) Variations in Tropical Sea Surface Temperature and
832 Surface Wind Fields Associated with the Southern Oscillation/El Niño. *Mon Weather*
833 *Rev* 110:354–384. doi: 10.1175/1520-0493(1982)110<0354:VITSST>2.0.CO;2

834 Suarez MJ, Schopf PS (1988) A Delayed Action Oscillator for ENSO. *J Atmos Sci*
835 45:3283–3287. doi: 10.1175/1520-0469(1988)045<3283:ADAOFE>2.0.CO;2

836 Trenberth KE, Caron JM (2001) Estimates of Meridional Atmosphere and Ocean Heat
837 Transports. *J Clim* 14:3433–3443. doi:
838 10.1175/1520-0442(2001)014<3433:EOMAAO>2.0.CO;2

839 Vecchi GA, Soden BJ (2007) Global Warming and the Weakening of the Tropical Circulation.
840 *J Clim* 20:4316–4340. doi: 10.1175/JCLI4258.1

841 Vecchi GA, Wittenberg AT (2010) El Niño and our future climate: where do we stand? *Wiley*
842 *Interdiscip Rev Clim Chang* 1:260–270. doi: 10.1002/wcc.33

843 Wang B, Zhang Q (2002) Pacific–East Asian Teleconnection. Part II: How the Philippine Sea
844 Anomalous Anticyclone is Established during El Niño Development*. *J Clim*

845 15:3252–3265. doi: 10.1175/1520-0442(2002)015<3252:PEATPI>2.0.CO;2

846 Wang C, Weisberg RH (1994) On the "slow mode" mechanism in the ENSO-related coupled
847 ocean- atmosphere models. *J. Clim.* 7:1657–1667.

848 Wang C, and Picaut J (2004) Understanding ENSO physics—A review. *Earth's Climate: The*
849 *Ocean-Atmosphere Interaction, Geophys. Monogr., Vol. 147, Amer. Geophys. Union,*
850 21 - 48

851 Wang W, McPhaden MJ (2000) The Surface-Layer Heat Balance in the Equatorial Pacific
852 Ocean. Part II: Interannual Variability*. *J Phys Oceanogr* 30:2989–3008. doi:
853 10.1175/1520-0485(2001)031<2989:TSLHBI>2.0.CO;2

854 Wang W, McPhaden MJ (2001) Surface Layer Temperature Balance in the Equatorial Pacific
855 during the 1997-98 El Niño and 1998-99 La Niña. *J Clim* 14:3393–3407. doi:
856 10.1175/1520-0442(2001)014<3393:SLTBIT>2.0.CO;2

857 Weisberg RH, Wang C (1997) Slow Variability in the Equatorial West-Central Pacific in
858 Relation to ENSO. *J Clim* 10:1998–2017. doi:
859 10.1175/1520-0442(1997)010<1998:SVITEW>2.0.CO;2

860 Xie S-P, Deser C, Vecchi G a., et al (2010) Global Warming Pattern Formation: Sea Surface
861 Temperature and Rainfall*. *J Clim* 23:966–986. doi: 10.1175/2009JCLI3329.1

862 Yang H, Wang F, Sun A (2009) Understanding the ocean temperature change in global
863 warming: the tropical Pacific. *Tellus A* 61:371–380. doi:
864 10.1111/j.1600-0870.2009.00390.x

865 Zebiak SE, Cane MA (1987) A Model El Niño–Southern Oscillation. *Mon Weather Rev*
866 115:2262–2278. doi: 10.1175/1520-0493(1987)115<2262:AMENO>2.0.CO;2

867 Zelle H, Jan van Oldenborgh G, Burgers G, Dijkstra H (2005) El Niño and Greenhouse
868 Warming: Results from Ensemble Simulations with the NCAR CCSM. *J Clim*
869 18:4669–4683. doi: 10.1175/JCLI3574.1

870 Zhang Q, Kumar A, Xue Y, et al (2007) Analysis of the ENSO Cycle in the NCEP Coupled
871 Forecast Model. *J Clim* 20:1265–1284. doi: 10.1175/JCLI4062.1

872 Zhang Q, Guan Y, Yang H (2008) ENSO amplitude change in observation and coupled

873 models. Adv Atmos Sci 25:361–366. doi: 10.1007/s00376-008-0361-5
874 Zhang X, McPhaden MJ (2006) Wind Stress Variations and Interannual Sea Surface
875 Temperature Anomalies in the Eastern Equatorial Pacific. J Clim 19:226–241. doi:
876 10.1175/JCLI3618.1

877

878 Captions of Table and Figures

879 **Table 1** Experiments with CESM1.1 and POP2

880 **Table 2** Annual mean values of the heat budget terms ($^{\circ}\text{C}/\text{year}$) during the 94-year
881 simulation period over the WEP region (135°E - 170°E , 5°S - 5°N) and the EEP region
882 (130°W - 80°W , 5°S - 5°N).

883 **Table 3** The correlation between FULL and overriding experiments of the heat budget terms
884 over the EEP region under GW.

885 **Fig. 1** Scatter plot of MLT anomaly and diffusion term averaged over the EEP.

886 **Fig. 2** Interannual variations of temperature simulated (T_i ; black) and reconstituted ($\text{Re}T_i$;
887 gray) from the heat budget defined as the sum of net surface heat flux (H ; green), zonal
888 ($-uT_x$; red), meridional ($-vT_y$; yellow), and vertical ($-wT_z$; blue) advection heat terms,
889 as well as the difference between the temperature simulated and reconstituted from this
890 heat budget (T_{diff} ; purple) for the top 55 m of (a) the WEP and (b) the EEP.

891 **Fig. 3** Monthly MLT anomaly at Nino3.4 region. The horizontal dashed line at 2.0°C is used
892 as the criterion to define the El Niño events. 17 El Niño events (red) are identified
893 during the 94-year simulation period.

894 **Fig. 4** Seasonal evolution of the El Niño composite at Nino3.4 region: (a) CPL85, (b) FULL
895 – CTRL (full response), (c) FULL – STRS (wind stress effect), (d) FULL – SPED
896 (wind speed effect), (e) WIND – CTRL (thermal warming effect). Pink area denotes the
897 upper and lower limits of the 17 composite members.

898 **Fig. 5** The El Niño- (left) and GW-induced (right) changes in the “El Niño year”:(a) & (b)
899 MLT, (c) & (d) wind stress and its magnitude, (e) & (f) zonal velocity averaged over
900 the top 55m, (g)&(h) vertical velocity at depth of 50 m, and (i) & (j) mixed layer

901 stratification. The GW-induced changes are their trends over 2006-2099 normalized by
902 multiplying 100 years, and the MLT in (b) is further normalized by subtracting the
903 mean value of field over 20°S – 20°N in the Pacific Ocean and then rescaled to
904 correspond to a 3°C increase. Superimposed are their climatological fields of the
905 corresponding variables in CPL85. The boxes in (a) represent the WEP (5°S-5°N,
906 135°E-170°E) and the EEP (5°S-5°N, 130°W-80°W) regions, respectively.

907 **Fig. 6** Seasonal evolution of anomalies during the El Niño composite (left) and GW (right)
908 along equator (between 2.5°S and 2.5°N): (a) & (b) MLT, (c) & (d) zonal wind stress,
909 (e) & (f) zonal velocity averaged over top 55m layers, (g) & (h) vertical velocity at
910 depth of 50 m, and (i) & (j) mixed layer stratification. The anomalies under GW are
911 their trends over 2006-2099 normalized by multiplying 100 years. Superimposed are
912 their climatological fields of the corresponding variables in CPL85.

913 **Fig. 7** The El Niño- (left) and GW-induced (right) changes in (a) & (b) MLT, (c) & (d) mixed
914 layer stratification, and (e) & (f) vertical velocity at depth of 50 m over the EEP in
915 CPL85 simulation (black), wind stress effect (FULL – STRS) (blue), and the thermal
916 warming effect (WIND – CTRL) (red).

917 **Fig. 8** Seasonal evolution of temperature anomalies along the equator (averaged between
918 2.5°S-2.5°N) during the El Niño composite (left) and GW (right). Superimposed are
919 the thermocline depths (thick purple lines from an average of 2006-2025; thick yellow
920 lines on the left-hand side panels from an average of the 17 El Niño composite
921 members, and thick yellow lines on the right-hand side panels from an average of
922 2080-2099) and the climatological temperature in CPL85 (black contours). The
923 thermocline depth is identified as the location of the maximum vertical gradient of
924 temperature.

925 **Fig. 9** The El Niño- (blue) and GW-induced (red) Pacific northward heat transports (NHT) in
926 (a) full response (FULL-CTRL), (b) wind stress effect (FULL – STRS), and (c) thermal
927 warming effect (WIND – CTRL). Black lines are the climatological Pacific NHTs in
928 CPL85.

929 **Fig. 10** The El Niño- (left) and GW-induced (right) changes in the Pacific meridional
930 overturning circulation (MOC) in (a) & (b) full response (FULL-CTRL), (c) & (d)
931 wind stress effect (FULL – STRS), and (e) & (f) thermal warming effect (WIND –
932 CTRL). Superimposed are the climatological Pacific MOCs in CPL85, and positive
933 (negative) values indicate a clockwise (counterclockwise) circulation.

934 **Fig. 12** Seasonal evolution of changes in the heat budget terms during El Niño (left) and GW
935 (right) along the equator (averaged between 2.5 °S and 2.5 °N): (a) & (b) temperature
936 tendency, (c) & (d) vertical advection, (e) & (f) zonal advection, (g) & (h) meridional
937 advection, (i) & (j) net surface heat flux, and (k) & (l) diffusion. Superimposed are
938 their climatological fields of the corresponding variables in CPL85.

939 **Fig. 13** The El Niño- (left) and GW-induced (right) changes over the EEP in (a) & (b)
940 temperature tendency, (c) & (d) vertical advection, (e) & (f) zonal advection, (g) & (h)
941 meridional advection, (i) & (j) net surface heat flux, and (k) & (l) diffusion from
942 CPL85 simulation (black), wind stress effect (FULL – STRS) (blue), and thermal
943 warming effect (WIND – CTRL) (red).

944 **Fig. 14** Schematic depicting the changes for El Niño (left) and GW (right). Color shading
945 indicates temperature anomalies at the sea surface (Northern Hemisphere only), along
946 140 °W in the latitude-depth sense, and along the equator in the longitude-depth plane
947 (averaged between 2.5 °S-2.5 °N). Superimposed are the thermocline depths similar to
948 those in Figs. 8i and 8j. The mean and anomalous circulation is represented by bold and
949 thin arrows, respectively.

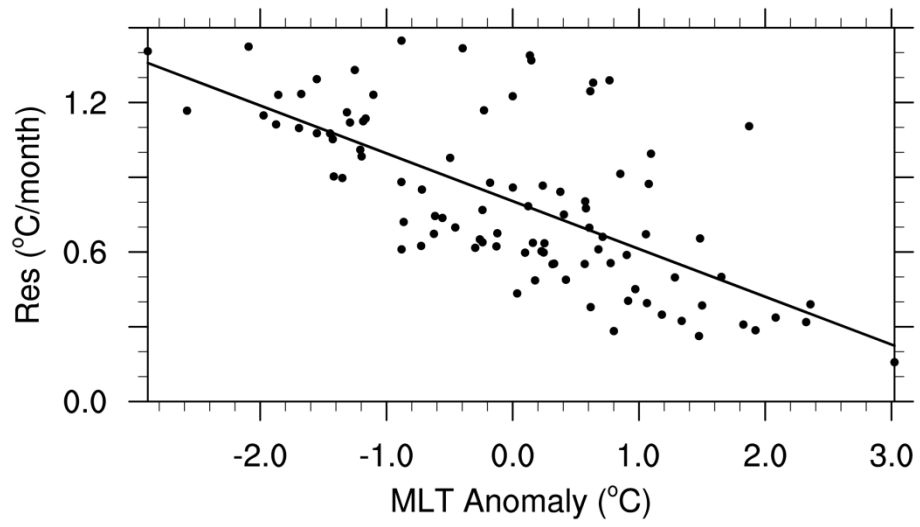


Fig. 1 Scatter plot of MLT anomaly and diffusion term averaged over the EEP.

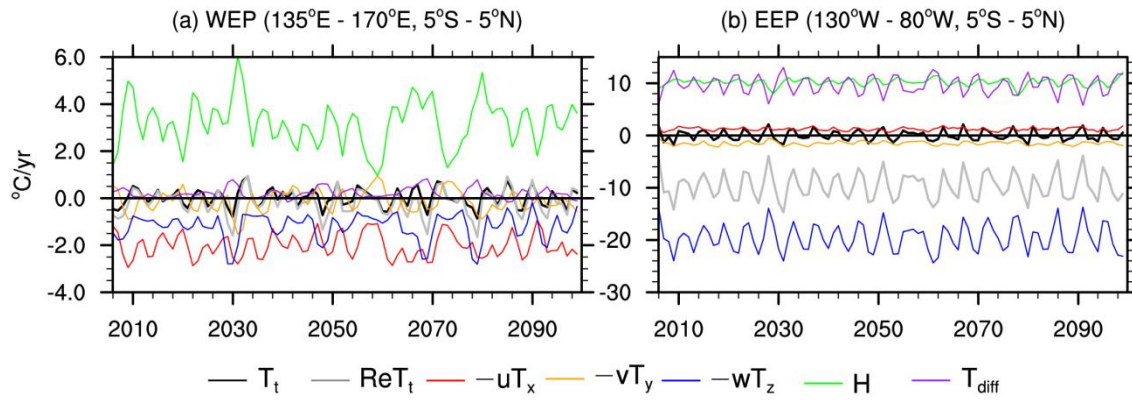


Fig. 2 Interannual variations of temperature simulated (T_t ; black) and reconstituted (ReT_t ; gray) from the heat budget defined as the sum of net surface heat flux (H ; green), zonal ($-uT_x$; red), meridional ($-vT_y$; yellow), and vertical ($-wT_z$; blue) advection heat terms, as well as the difference between the temperature simulated and reconstituted from this heat budget (T_{diff} ; purple) for the top 55 m of (a) the WEP and (b) the EEP.

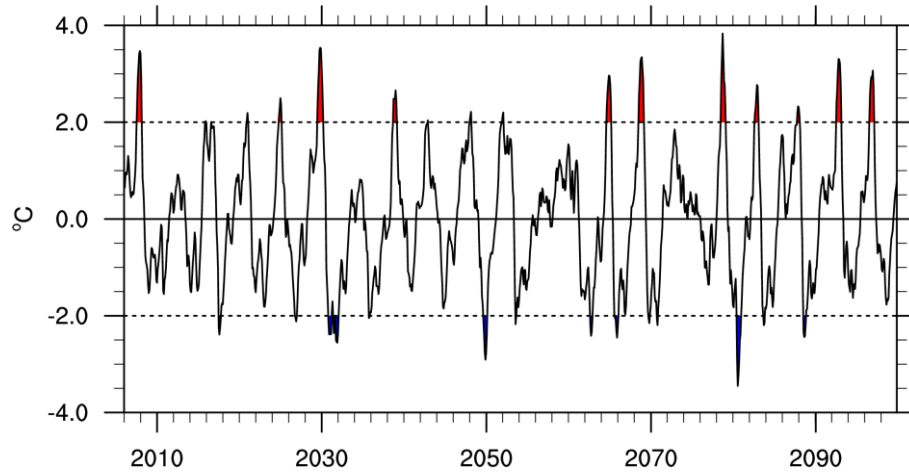


Fig. 3 Monthly MLT anomaly at Nino3.4 region. The horizontal dashed line at 2.0 °C is used as the criterion to define the El Niño events. 17 El Niño events (red) are identified during the 94-year simulation period.

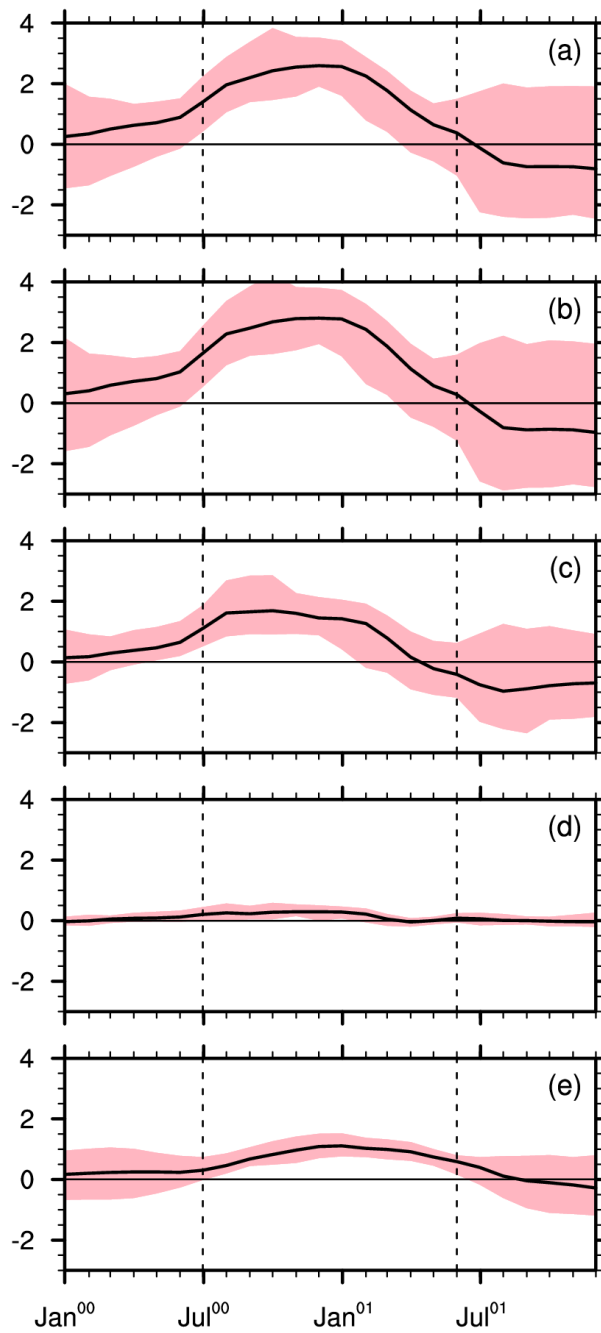


Fig. 4 Seasonal evolution of the El Niño composite at Nino3.4 region: (a) CPL85, (b) FULL – CTRL (full response), (c) FULL – STRS (wind stress effect), (d) FULL – SPED (wind speed effect), (e) WIND – CTRL (thermal warming effect). Pink area denotes the upper and lower limits of the 17 composite members.

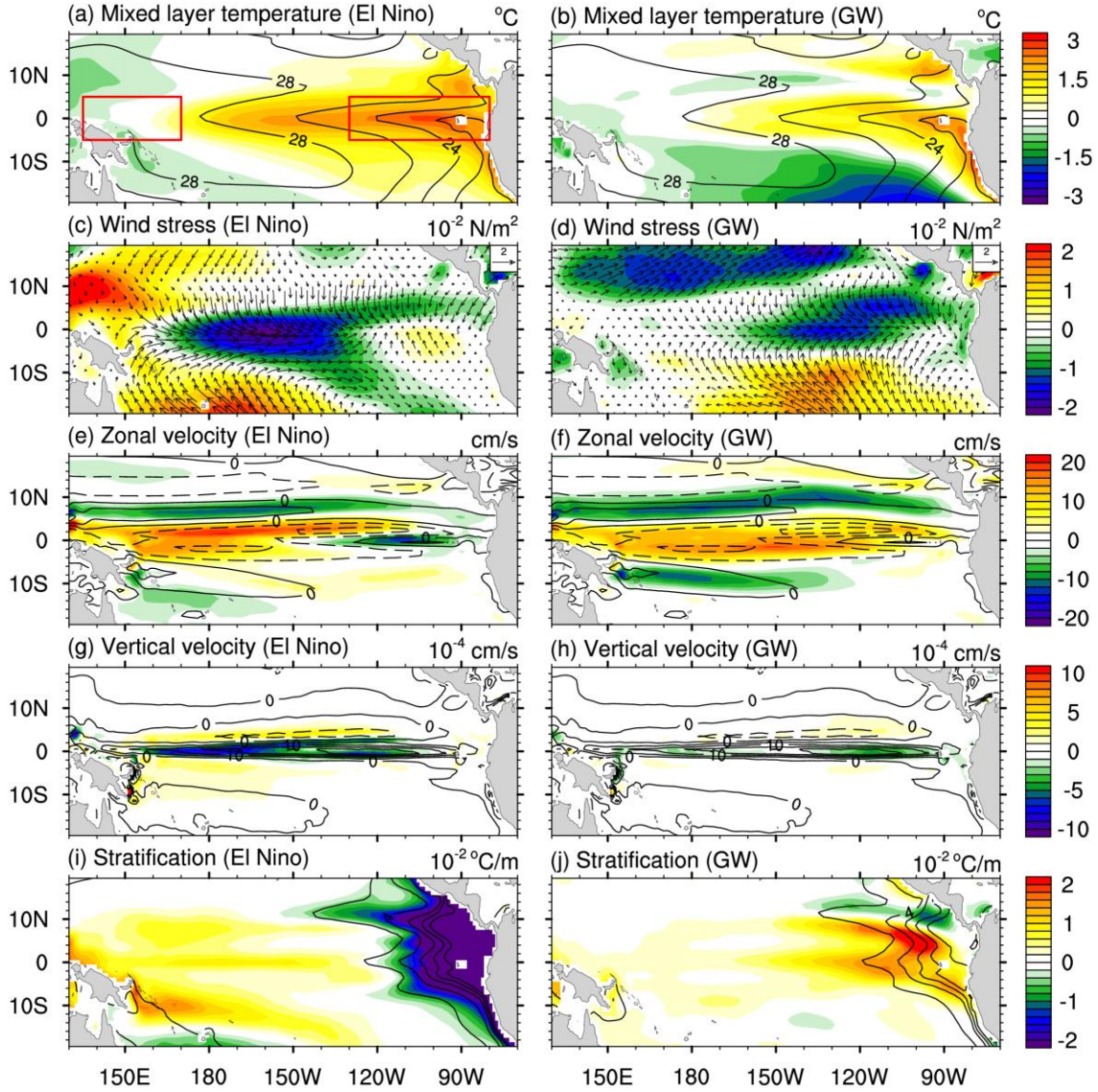


Fig. 5 The El Niño- (left) and GW-induced (right) changes in the “El Niño year”: (a) & (b) MLT, (c) & (d) wind stress and its magnitude, (e) & (f) zonal velocity averaged over the top 55m, (g)&(h) vertical velocity at depth of 50 m, and (i) & (j) mixed layer stratification. The GW-induced changes are their trends over 2006-2099 normalized by multiplying 100 years, and the MLT in (b) is further normalized by subtracting the mean value of field over 20°S – 20°N in the Pacific Ocean and then rescaled to correspond to a 3 °C increase. Superimposed are their climatological fields of the corresponding variables in CPL85. The boxes in (a) represent the WEP (5°S-5°N, 135°E-170°E) and the EEP (5°S-5°N, 130°W-80°W) regions, respectively.

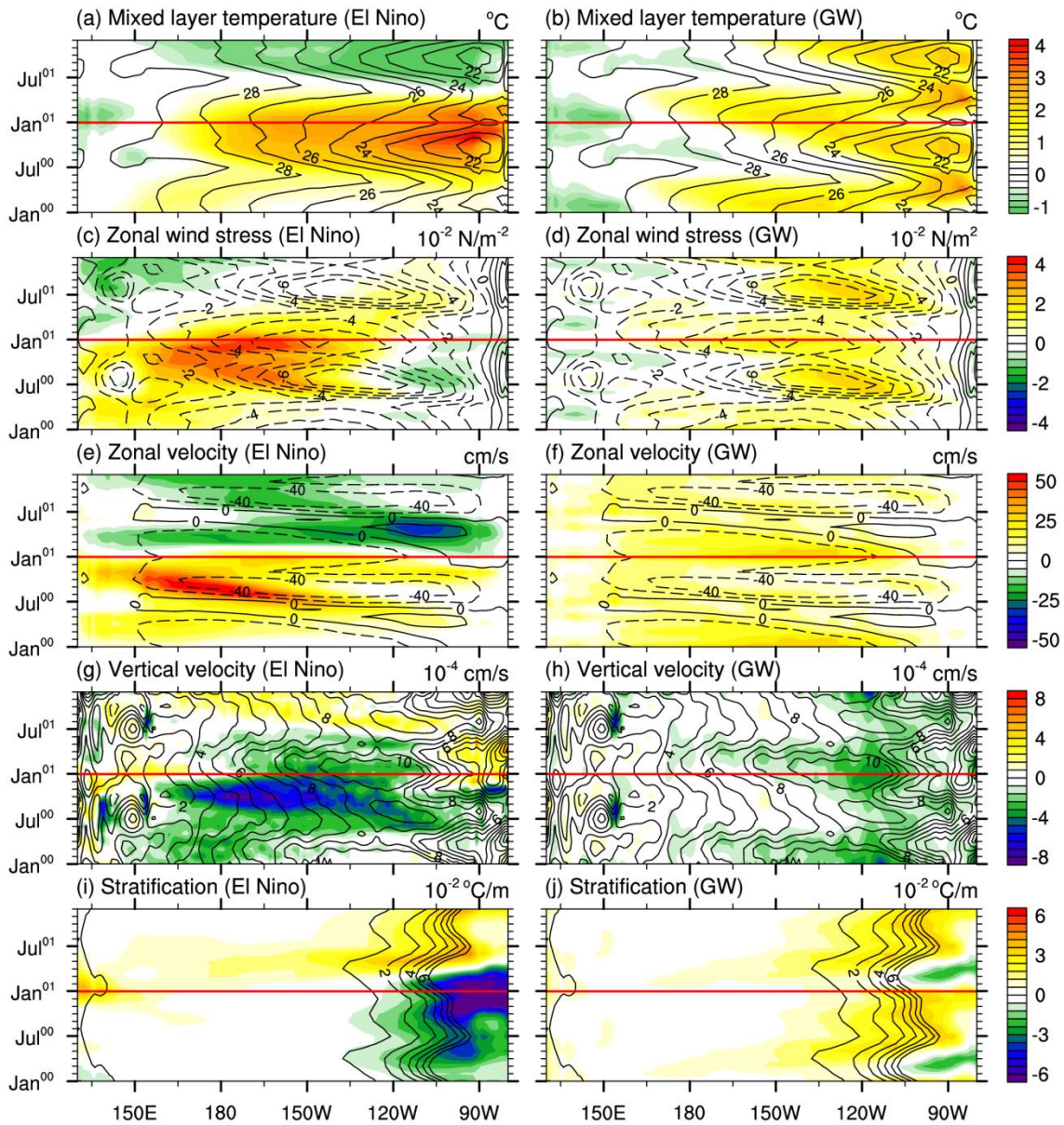


Fig. 6 Seasonal evolution of anomalies during the El Niño composite (left) and GW (right) along equator (between 2.5°S and 2.5°N): (a) & (b) MLT, (c) & (d) zonal wind stress, (e) & (f) zonal velocity averaged over top 55m layers, (g) & (h) vertical velocity at depth of 50 m, and (i) & (j) mixed layer stratification. The anomalies under GW are their trends over 2006-2099 normalized by multiplying 100 years. Superimposed are their climatological fields of the corresponding variables in CPL85.

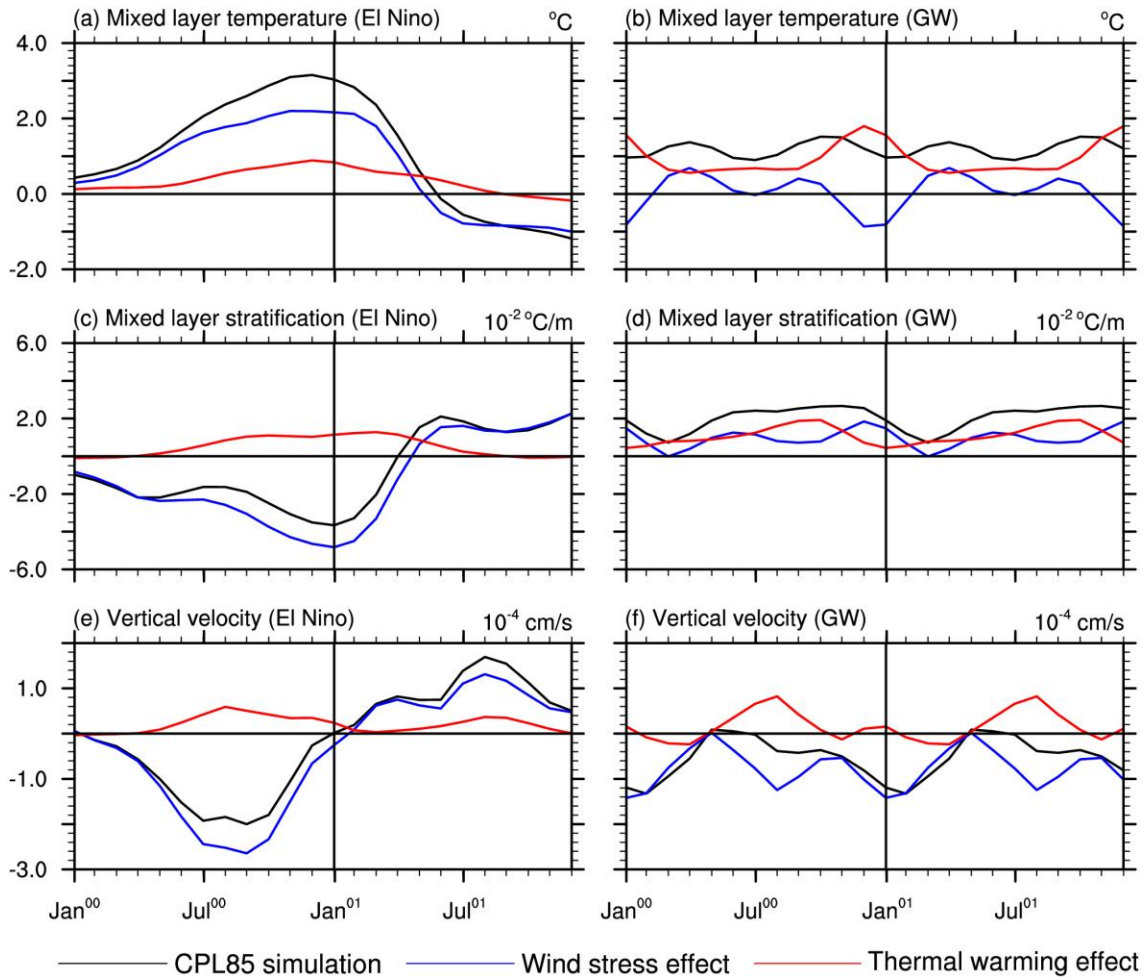


Fig. 7 The El Niño- (left) and GW-induced (right) changes in (a) & (b) MLT, (c) & (d) mixed layer stratification, and (e) & (f) vertical velocity at depth of 50 m over the EEP in CPL85 simulation (black), wind stress effect (FULL – STRS) (blue), and the thermal warming effect (WIND – CTRL) (red).

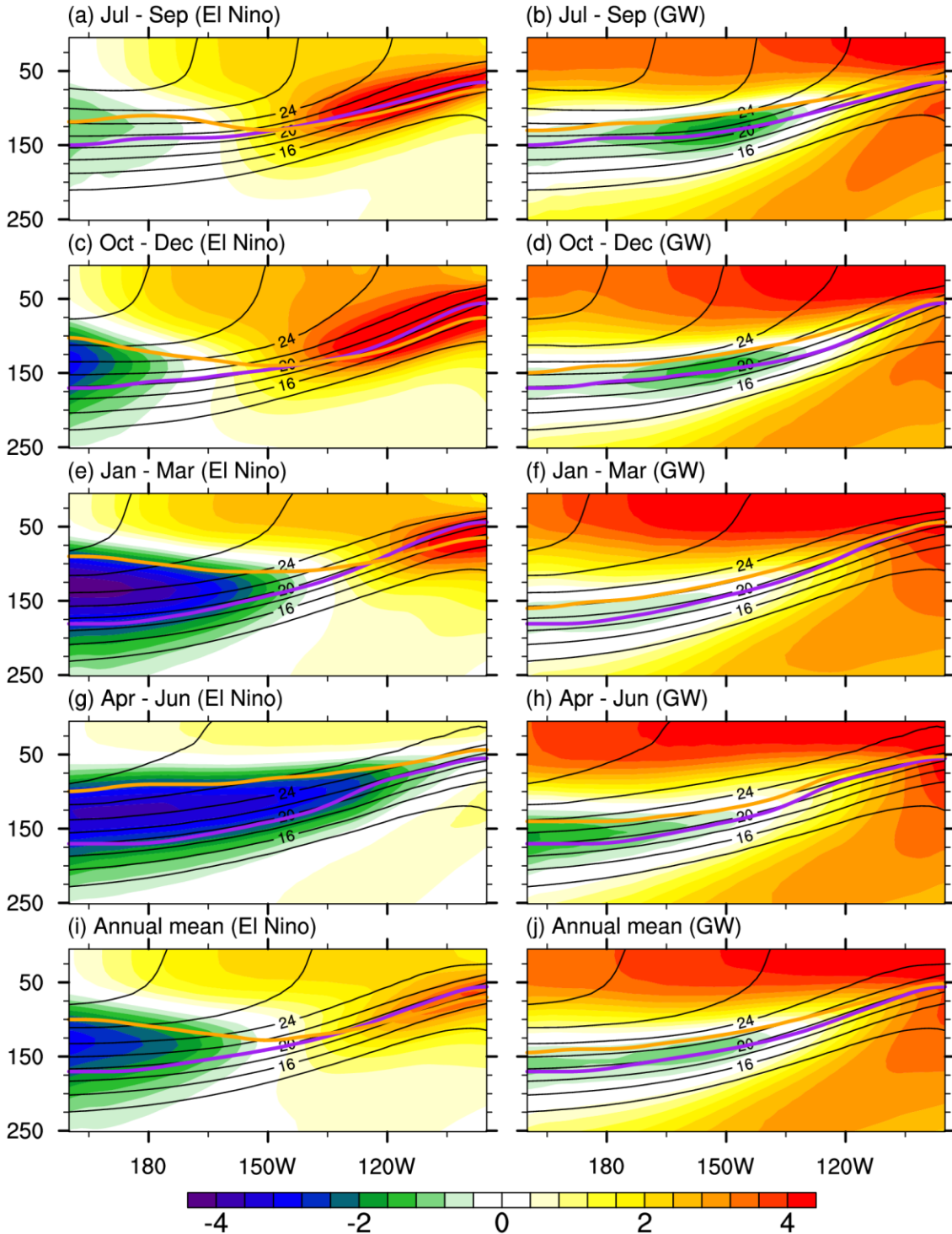


Fig. 8 Seasonal evolution of temperature anomalies along the equator (averaged between 2.5°S-2.5°N) during the El Niño composite (left) and GW (right). Superimposed are the thermocline depths (thick purple lines from an average of 2006-2025; thick yellow lines on the left-hand side panels from an average of the 17 El Niño composite members, and thick yellow lines on the right-hand side panels from an average of 2080-2099) and the climatological temperature in CPL85 (black contours). The thermocline depth is identified as the location of the maximum vertical gradient of temperature.

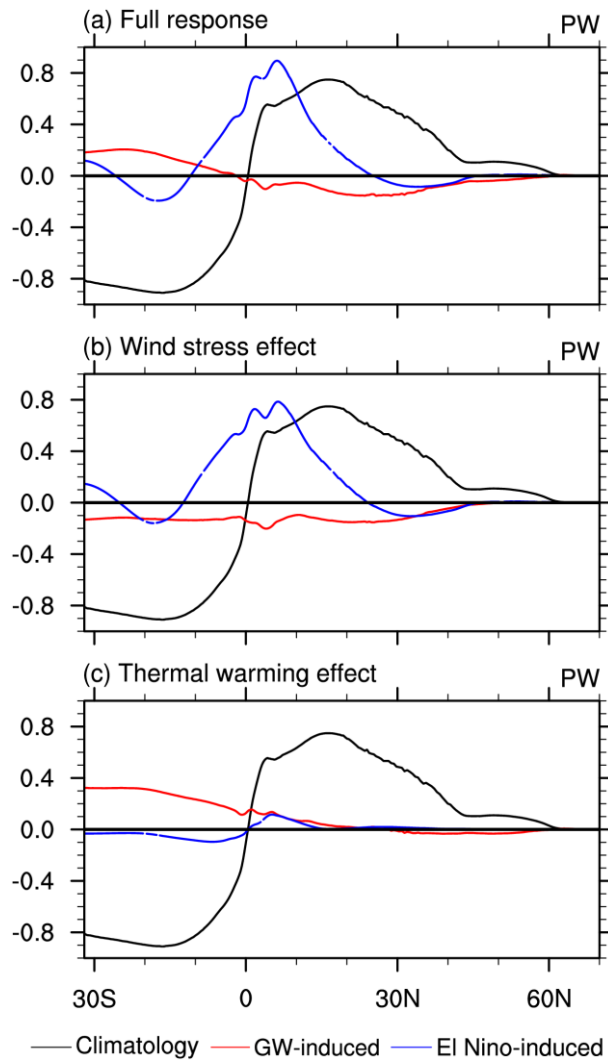


Fig. 9 The El Niño- (blue) and GW-induced (red) Pacific northward heat transports (NHT) in (a) full response (FULL-CTRL), (b) wind stress effect (FULL – STRS), and (c) thermal warming effect (WIND – CTRL). Black lines are the climatological Pacific NHTs in CPL85.

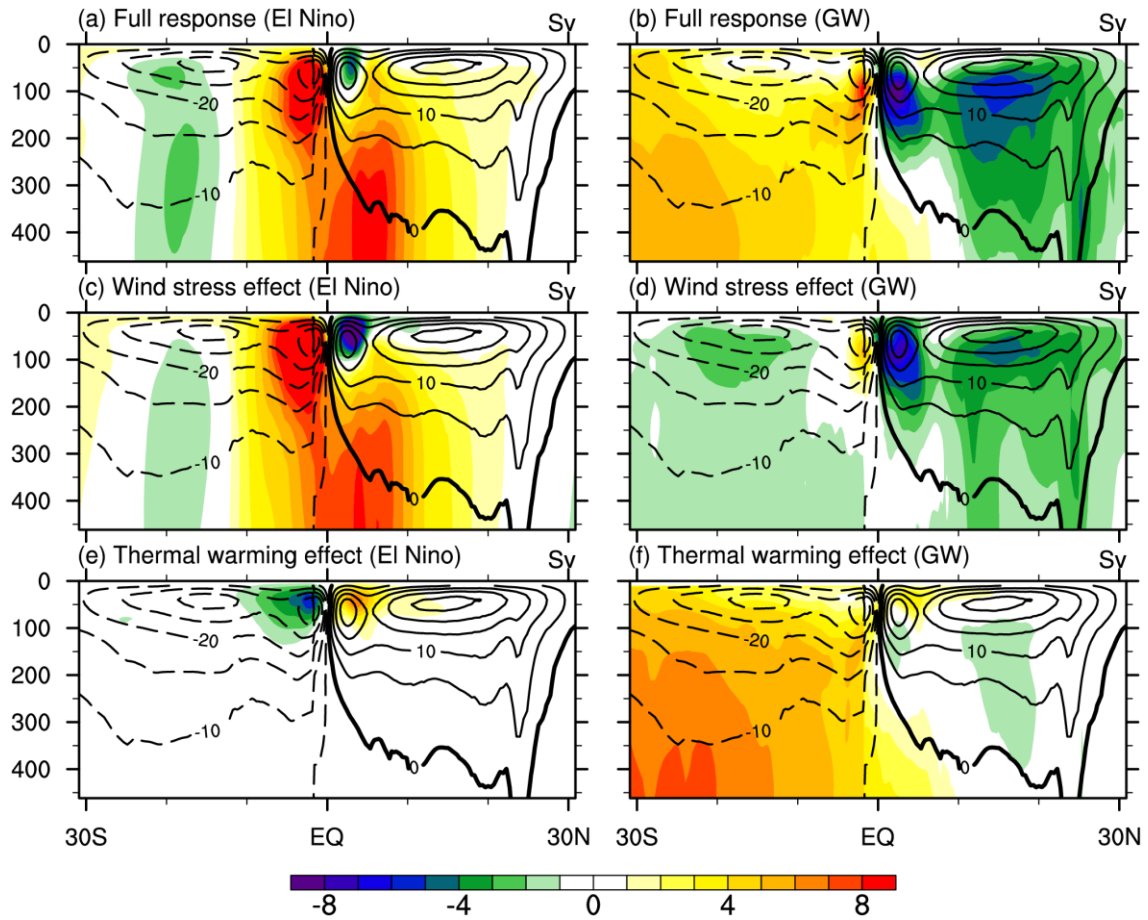


Fig. 10 The El Niño- (left) and GW-induced (right) changes in the Pacific meridional overturning circulation (MOC) in (a) & (b) full response (FULL-CTRL), (c) & (d) wind stress effect (FULL – STRS), and (e) & (f) thermal warming effect (WIND – CTRL). Superimposed are the climatological Pacific MOCs in CPL85, and positive (negative) values indicate a clockwise (counterclockwise) circulation.

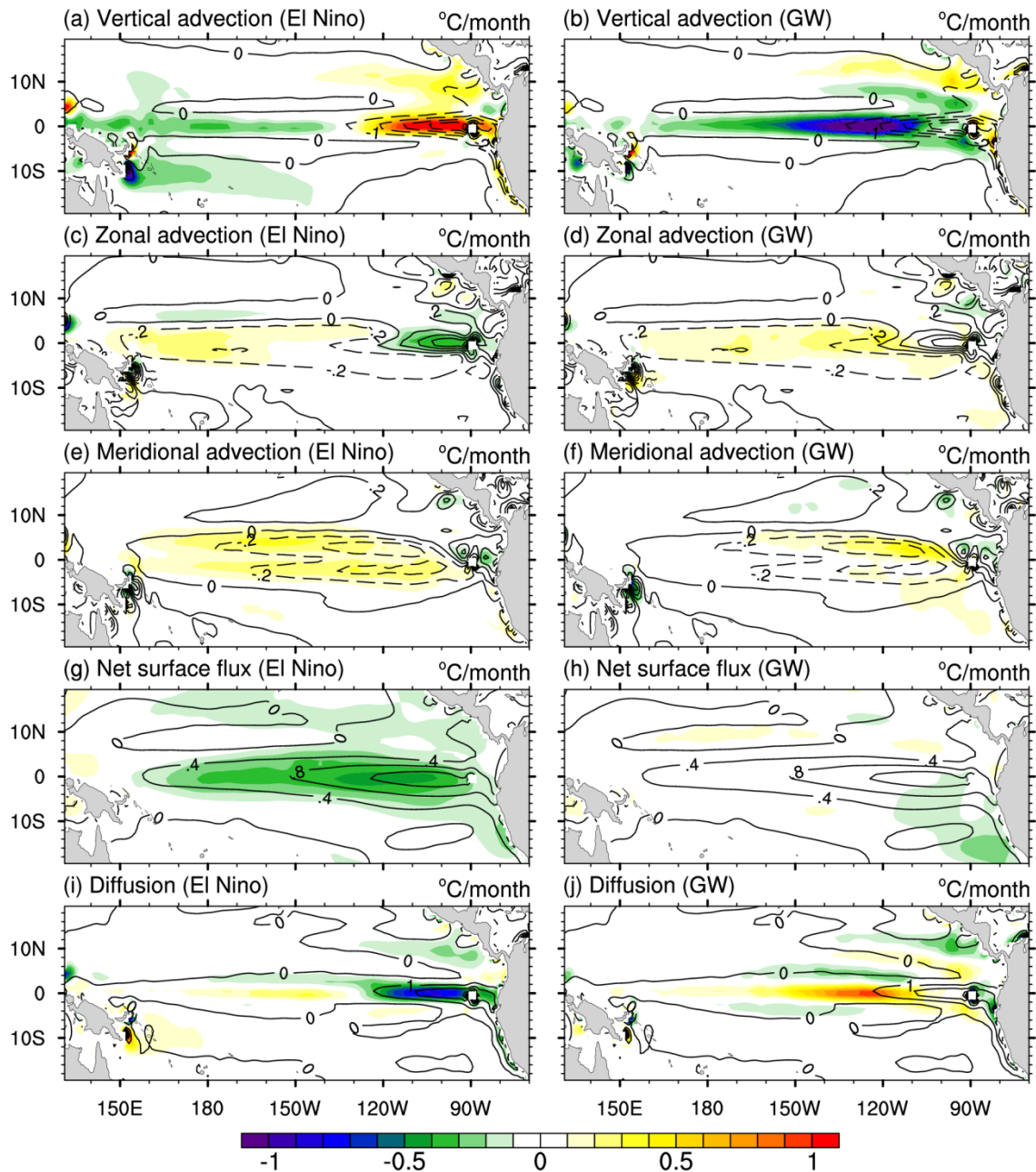


Fig. 11 The El Niño- (left) and GW-induced (right) changes in the heat budget terms during the “El Niño year”: (a) & (b) vertical advection, (c) & (d) zonal advection, (e) & (f) meridional advection, (g) & (h) net surface heat flux, and (i) & (j) diffusion. Superimposed are their climatological fields of the corresponding variables in CPL85.

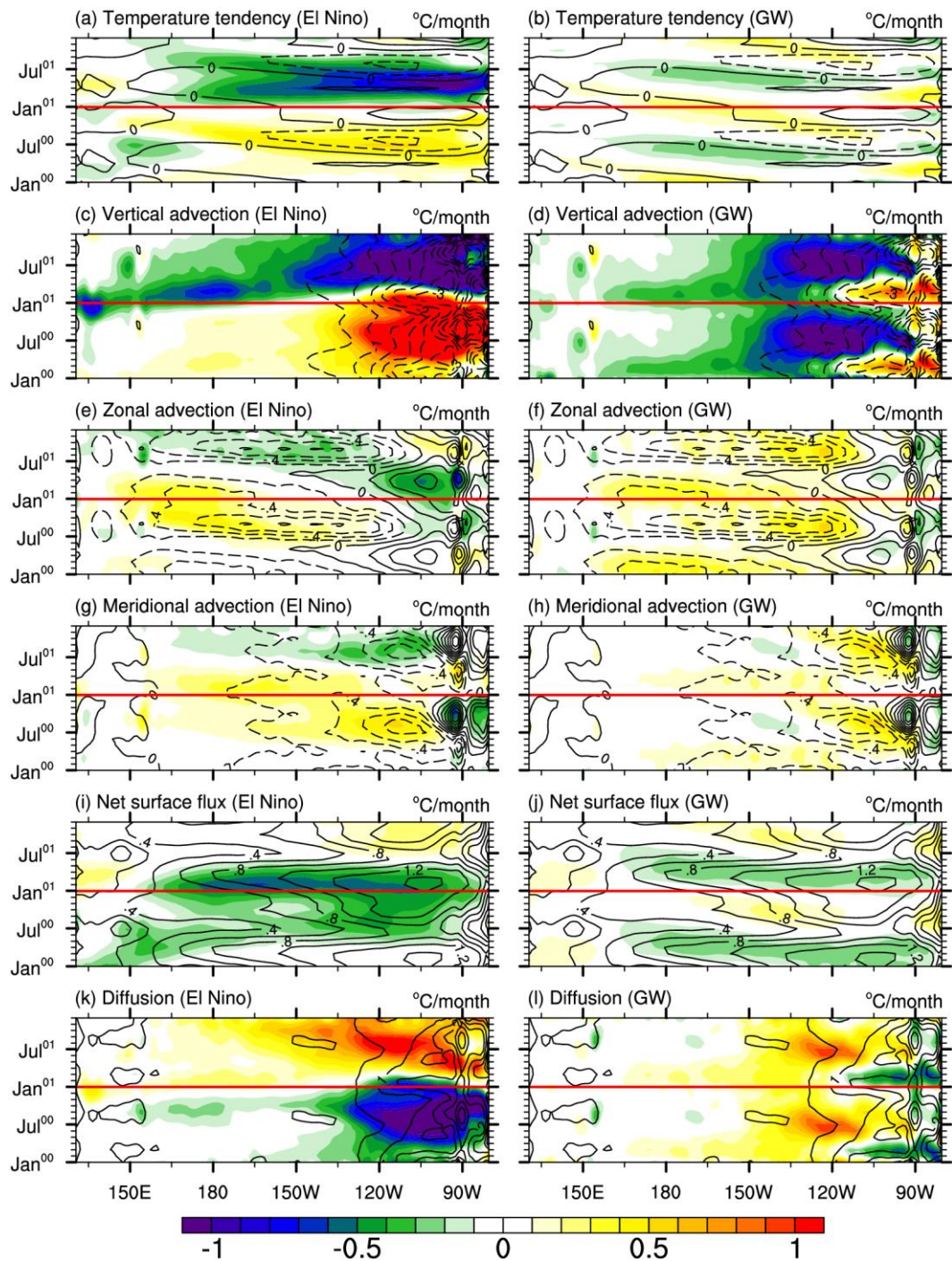


Fig. 12 Seasonal evolution of changes in the heat budget terms during El Niño (left) and GW (right) along the equator (averaged between 2.5°S and 2.5°N): (a) & (b) temperature tendency, (c) & (d) vertical advection, (e) & (f) zonal advection, (g) & (h) meridional advection, (i) & (j) net surface heat flux, and (k) & (l) diffusion. Superimposed are their climatological fields of the corresponding variables in CPL85.

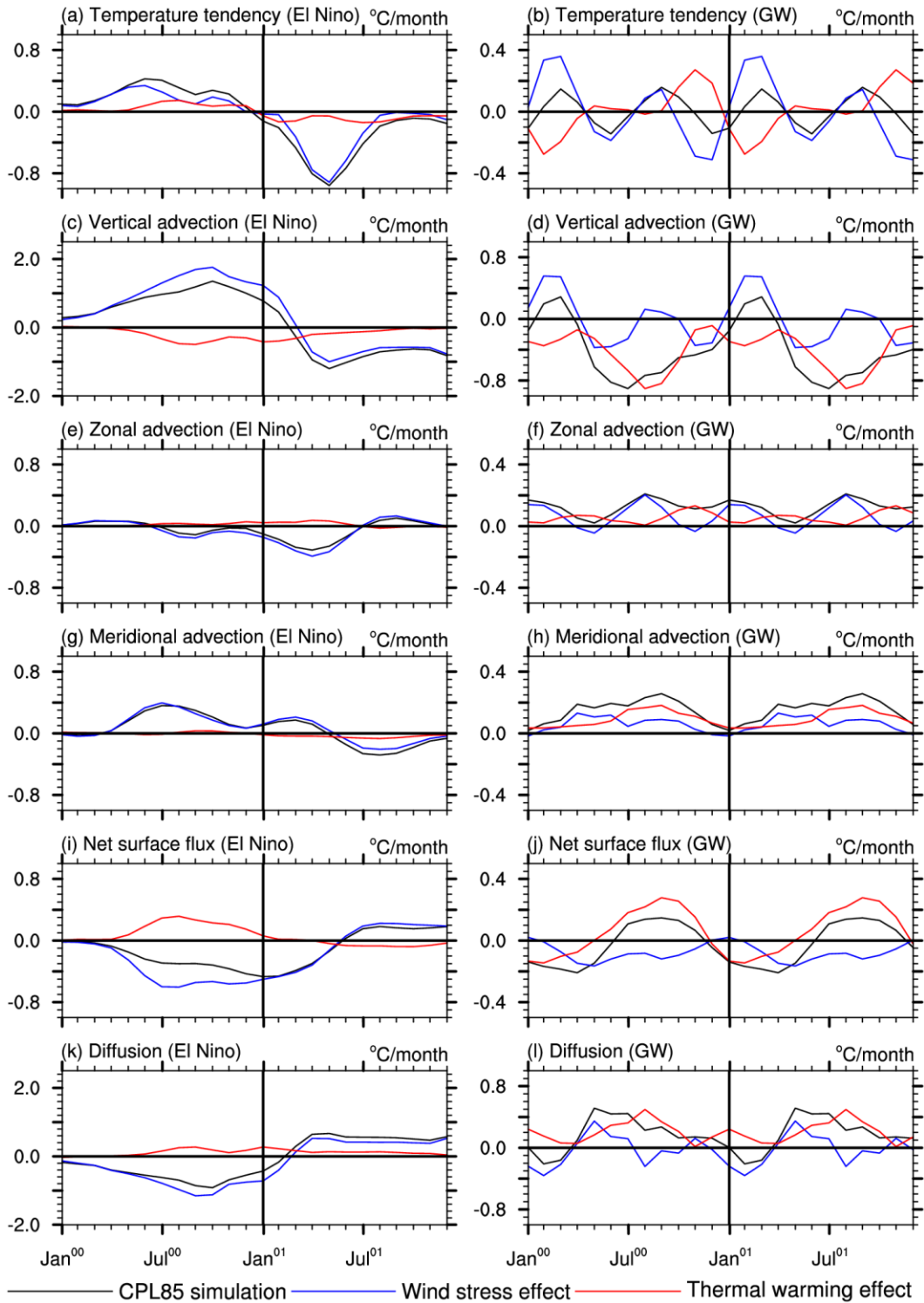


Fig. 13 The El Niño- (left) and GW-induced (right) changes over the EEP in (a) & (b) temperature tendency, (c) & (d) vertical advection, (e) & (f) zonal advection, (g) & (h) meridional advection, (i) & (j) net surface heat flux, and (k) & (l) diffusion from CPL85 simulation (black), wind stress effect (FULL – STRS) (blue), and thermal warming effect (WIND – CTRL) (red).

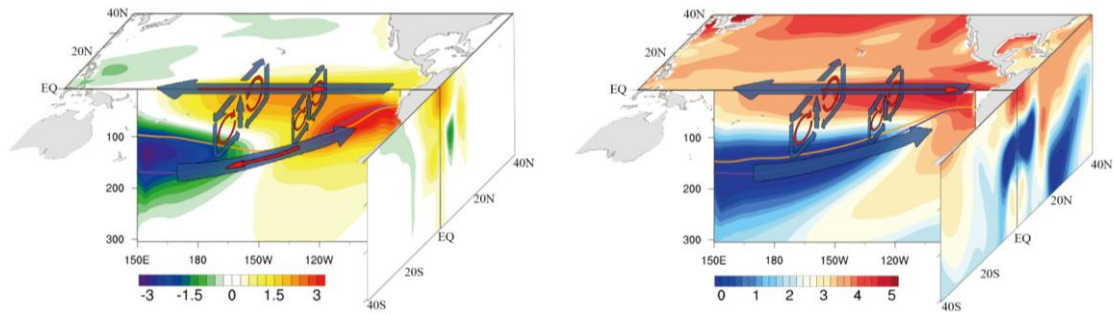


Fig. 14 Schematic depicting the changes for El Niño (left) and GW (right). Color shading indicates temperature anomalies at the sea surface (Northern Hemisphere only), along 140°W in the latitude-depth sense, and along the equator in the longitude-depth plane (averaged between 2.5°S-2.5°N). Superimposed are the thermocline depths similar to those in Figs. 8i and 8j. The mean and anomalous circulation is represented by bold and thin arrows, respectively.

1
2**Table 1** Experiments with CESM1.1 and POP2

NAME	RUN (yrs.)	DESCRIPTION
CPL85	94	RCP8.5 simulation with NCAR's Community Earth System Model from 2006 to 2099
FULL	94	POP2 is integrated from 2006 to 2099 with daily wind stress and fluxes from CESM
CTRL	94	POP2 is forced repeatedly by the 2006 daily wind stress and fluxes from CESM
STRS	94	Same as FULL, but wind stress is specified to that of 2006
SPED	94	Same as FULL, but wind speed is specified to that of 2006 through bulk formula
WIND	94	Same as FULL, but both wind stress and wind speed are specified to those of 2006

3

4 **Table 2** Annual mean values of the heat budget terms ($^{\circ}\text{C}$ /year) during the 94-year
 5 simulation period over the WEP region (135°E - 170°E , 5°S - 5°N) and the EEP region
 6 (130°W - 80°W , 5°S - 5°N).

Term Region	T_t	$\text{Re}T_t$	$-wT_z$	$-uT_x$	$-vT_y$	H	T_{diff}
WEP	0.02	-0.18	-1.21	-2.02	-0.14	3.20	0.15
EEP	0.04	-9.62	-19.53	1.21	-1.50	10.20	9.58

7
8

9 **Table 3** The correlation between FULL and overriding experiments of the heat budget terms
 10 over the EEP region under GW.
 11

Term Correlation	$-wT_z$	$-uT_x$	$-vT_y$	H	T_{diff}
FULL and WS	0.76	0.86	0.81	-0.11	0.81
FULL and TW	0.56	-0.41	0.77	0.96	0.44
WS and TW	-0.11	-0.81	0.27	-0.39	-0.16

12